A&A 617, A63 (2018)
https://doi.org/10.1051/0004-6361/201833172

Astronomy & Astrophysics

Low-mass star formation and subclustering in the H II regions RCW 32, 33, and 27 of the Vela Molecular Ridge

A photometric diagnostics for identifying M-type stars⋆

L. Prisinzano[1], F. Damiani[1], M. G. Guarcello[1], G. Micela[1], S. Sciortino[1], E. Tognelli[2], and L. Venuti[1]

[1] INAF – Osservatorio Astronomico di Palermo, Piazza del Parlamento 1, 90134 Palermo, Italy
e-mail: loredana.prisinzano@inaf.it
[2] Department of Physics "E. Fermi", University of Pisa, Largo Bruno Pontecorvo 3, 56127 Pisa, Italy

Received 6 April 2018 / Accepted 14 June 2018

ABSTRACT

Context. Most stars are born in clusters, and recent results suggest that star formation (SF) preferentially occurs in subclusters. Studying the morphology and SF history of young clusters is crucial for understanding early cluster formation processes.
Aims. We aim to identify the embedded population of young stellar objects (YSOs) down to the low-mass stars in the M-type regime in the three H II regions RCW 33, RCW 32, and RCW 27, which are located in the northwestern region of the Vela Molecular Ridge. Our aim is to characterize their properties, such as morphology and extent of the clusters in the three H II regions, derive stellar ages, and determine the connection of the SF history with the environment.
Methods. Through public photometric surveys such as *Gaia*, VPHAS+, 2MASS, and *Spitzer*/GLIMPSE, we identify YSOs with classical techniques aimed at detecting IR, Hα, and UV excesses as signatures of circumstellar disks and accretion. In addition, we implement a method for distinguishing main-sequence (MS) stars and giants in the M-type regime by comparing the reddening derived in several optical/IR color-color diagrams, assuming suitable theoretical models. Since this diagnostic is sensitive to stellar gravity, the procedure allows us to also identify pre-MS (PMS) stars.
Results. Using the classical membership criteria, we find that a large population of YSOs shows signatures of circumstellar disks with or without accretion. In addition, with the new technique of M-type star selection, we find a rich population of young M-type stars whose spatial distribution strongly correlates with the more massive population. We find evidence of three young clusters, with different morphology, for which we estimate the individual distances using TGAS *Gaia* data of the brighter subsample. In addition, we identify field stars falling in the same region by securely classifying them as giants and foreground MS stars.
Conclusions. We identify the embedded population of YSOs down to about 0.1 $M_{\odot}$ that is associated with the three H II regions RCW 33, RCW 32, and RCW 27 and the three clusters Vela T2, Cr 197, and Vela T1, respectively. All the three clusters are located at a similar distance, but they have very different morphologies. Our results suggest a decreasing SF rate in Vela T2 and triggered SF in Cr 197 and Vela T1.

Key words. techniques: photometric – stars: low-mass – stars: pre-main sequence – stars: formation – H II regions – open clusters and associations: general

1. Introduction

The Vela Molecular Ridge (VMR) is a large molecular cloud complex revealed by four strong emission peaks observed in the 1→0 transition of ^{12}CO (Murphy & May 1991), indicating that active SF is taking place (Pettersson 2008). It is located in the constellations of Puppis and Vela, and it is part of a complex region including the very large H II Gum Nebula, the Vela supernova remnant, and also a remarkable annular system of cometary globules (Pettersson 2008).

Murphy & May (1991) identified four main clouds within the VMR, called A, B, C, and D. Clouds A, C, and D are located at 0.7 ± 0.2 kpc, and cloud B is located at 2 kpc. Several small H II regions have also been found in this region. Liseau et al. (1992) and Lorenzetti et al. (1993) have found 33 Class I objects in the VMR based on JHKL near-infrared (NIR) photometry, of which 25 lie in clouds A, C, and D and 8 in cloud B. Other surveys based on NIR and CO observations have been conducted in the whole VMR region with the aim of finding signs of embedded young stellar objects (YSOs). A detailed review is given in Pettersson (2008).

The northwestern region of the VMR, which lies in cloud D, has been the subject of an Hα survey covering a $5\overset{\circ}{.}5 \times 5\overset{\circ}{.}5$ field, centered on RA (1950) = $8^{\rm h}43^{\rm m}.2$, Dec (1950) = $-40^{\circ}57'$, as reported by Pettersson & Reipurth (1994). The three H II regions, RCW 27, 32, and 33, where signatures of recent low-mass star formation (SF) have been found by these authors, is one of the peculiarities of this field. The authors identified 278 Hα emission objects (with a completeness limit $V = 19$) associated with dark clouds and the three H II regions. In particular, they found two main concentrations, called Vela T1 and Vela T2 T Tauri associations, toward the H II regions RCW 27 and RCW 33, respectively. They also took slit spectra of 24 of the emission-line stars and found that the majority have a spectral appearance similar to T Tauri stars.

⋆ Full Tables 2 and 3 are only available at the CDS via anonymous ftp to http://cdsarc.u-strasbg.fr (130.79.128.5) or via http://cdsarc.u-strasbg.fr/viz-bin/qcat?J/A+A/617/A63

Yamaguchi et al. (1999a) attempted to assign a possible age sequence, suggesting that the sparse Vela T1 association in RCW 27 is more evolved than the tighter Vela T2 association in RCW 33. They explained this sequential SF as an effect of the influence of the exciting OB stars on the molecular clouds.

Massi et al. (1999, 2003) have carried out deep JHK imaging and 1.3 mm continuum photometry of 15 of the Class I sources found in the VMR D, while Testi et al. (2001) and Massi et al. (2006) have obtained deep JHKs images of six of the most luminous IRAS sources in the VMR D cloud. They found evidence of embedded clusters younger than 1 Myr for which they derived initial mass functions that are consistent with those derived for field stars and clusters.

RCW 32 is likely excited by HD 74804, the brightest star of Collinder 197 (Cr 197). The Hα emission stars in this region are very concentrated. It has been the target of a deeper objective prism image and of a ROSAT HRI observation, which identified 70 and 30 YSOs, respectively. Several embedded sources were found in the region, which suggests an age of 1 Myr. The young galactic cluster Cr 197 has been the subject of a dynamical study by Bonatto & Bica (2010), who found it in a supervirial state, with evidence of some deviation from dynamical equilibrium.

Several studies, dedicated to individual sources lying in the northern region of the VMR, provide significantly different distances in the range 0.70–1.15 kpc (see Pettersson & Reipurth 1994, for a review). More recently, a distance of 0.85 kpc has been attributed to the cluster, called ASCC 50, that was detected in RCW 33 by Kharchenko et al. (2005) and confirmed by Kharchenko et al. (2013).

In this work, we wish to study the northern region of the VMR that was covered by Pettersson & Reipurth (1994) to understand the connection between the star-forming sites found in it and the SF history. In particular, we aim at characterizing and comparing the properties of the three embedded young clusters Vela T2 (corresponding to ASCC 50), Cr 197, and Vela T1, associated with RCW 33, RCW 32, and RCW 27, respectively.

To this aim, we exploit the potential of recently public data such as the deep optical-Hα VPHAS+ survey and the available NIR and X-ray data complemented by the new *Gaia* astrometric and kinematic data. This will allow us to perform a global analysis of the region by assessing the properties of the three subclusters, from which we hope to derive hints on the SF process.

The paper is organized as follows. Section 2 describes the photometric catalog we assembled and used for this study. In Sect. 3 we describe the selection of accreting YSOs, and in Sect. 4 we describe the selection of YSOs with a circumstellar disk. In Sect. 5 we describe the kinematic analysis of the TGAS *Gaia* data, while in Sect. 6 we summarize the properties of the members we selected with classical methods. In Sect. 7 we illustrate the procedure we adopted to identify M-type stars, derive their reddening, and identify M-type giants, MS stars, and cluster members. In Sect. 8 we discuss our results on the spatial distribution and the SF history, while our conclusions are summarized in Sect. 9.

2. Catalog compilation

Figure 1 shows an Hα image of $6^\circ \times 6^\circ$centered at (RA, Dec) = (131°, −41°) taken from the Southern H-Alpha Sky Survey Atlas (Gaustad et al. 2001). It includes the northwestern region of the VMR we study here that we label as NW-VMR region. The three areas in the three H II regions RCW 33, RCW 32 and RCW 27, respectively, centered on RA (J2000) = [132.°73, 131.°2,129.°5] deg and Dec (J2000) = [−42.°13,−41.°3,−40.°6] are the subject of this work.

The NW-VMR is included in the VST Photometric Hα Survey of the Southern Galactic Plane (VPHAS+ Drew et al. 2014). We used photometry of Data Release 2 (Date: 2015-07-30) from the ESO Catalog Facility within a radius of 3°around (RA, Dec) = (131°, −41°). This multiband source catalog has been obtained from observations of the OmegaCAM CCD imager mounted on the 2.6 m VLT Survey Telescope (VST) on Cerro Paranal, Chile. Imaging is performed with the IMAGE/OFFSET technique using the bands *u*_SDSS, *g*_SDSS, *r*_SDSS, *i*_SDSS, and NB_659, corresponding to the five filters *u, g, r, i,* and Hα, down to $r \sim 21$.

From this catalog, we selected objects tagged as the best available detections per unique object, with a signal-to-noise ratio (S/N) > 10 and a DAOPHOT (Stetson 1987) point spread function fitting score of CHI <1.5 in the *r*, *i*, and Hα bands. With this selection, the VPHAS+ catalog in NW-VMR includes 499 664 objects with photometric errors smaller than 0.1 mag. Since the observations with the *u* and *g* filters cover only the northwestern part of RCW 27, we did not consider the *u* and *g* magnitudes.

VPHAS+ magnitudes are given both in the Vega and AB system (Oke & Gunn 1983). A detailed description of the survey strategy, photometric offsets, photometric quality, exposure times, and pipeline used to derive the magnitudes can be found in Drew et al. (2014).

The deep VPHAS+ photometric catalog ranges from $g = 13$ down to $g \sim 21$. Magnitudes $g < 13$ are affected by saturation (Drew et al. 2014). For this reason, we compiled the photometric catalog of the NW-VMR region using the VPHAS+ catalog for $r \geq 13$ and the AAVSO[1] Photometric All-Sky Survey (APASS) DR9 (Henden et al. 2016) catalog for $r < 13$. To check the VPHAS+ calibration, we cross-matched the APASS magnitudes, calibrated in the SDSS[2] AB system, with the VPHAS+ catalog by considering objects with $14 < r < 17$, both in the VPHAS+ and APASS catalog. These limits have been chosen to avoid saturated objects in the VPHAS+ catalog and large errors in the APASS catalog whose limiting magnitude is about $r = 17.8$ mag. Using a matching radius of 1″, we computed the systematic shift between the astrometric systems of the two catalogs corresponding to $RA_{VPHAS} - RA_{APASS} = 0.''07$ and $Dec_{VPHAS+} - Dec_{APASS} = 0.''05$. We corrected the APASS coordinates for this shift and again cross-correlated the two catalogs by adopting a matching radius of 0.″5. The 5 982 objects common to the VPHAS+ and APASS catalogs were used to check the VPHAS+ photometry. By considering the range $0.2 < r-i < 1.5$, comprising the bulk of objects of our interest, we find that the *r* and *i* magnitude differences between VPHAS+ and APASS catalogs do not show any dependence on the relevant colors, while the median offsets are 0.009 and −0.020 mag in the *i* and *r* bands, respectively. Since these are negligible with respect to the photometric errors, we do not apply any correction to the magnitudes. The final optical catalog includes 568 811 entries in NW-VMR.

The NIR counterparts of the objects included in our optical catalog were found in the 2MASS Point Sources catalog (Cutri et al. 2003), from which we selected only objects with photometric quality flag "A" in at least one of the three

[1] American Association of Variable Star Observers.
[2] Sloan Digital Sky Survey.

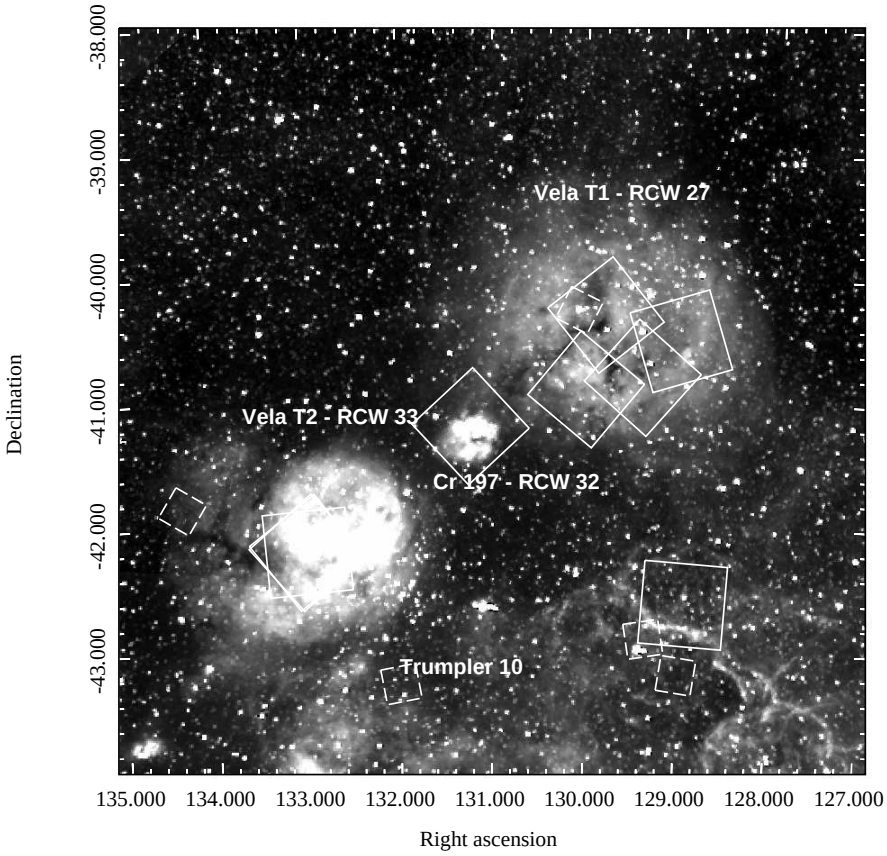

Fig. 1. $6° \times 6°$ Hα image centered on (RA, Dec) = (131, −41), taken from the Southern H-Alpha Sky Survey Atlas (Gaustad et al. 2001). The positions of Trumpler 10 and of the three H II regions are indicated. The FOVs of the ROSAT HRI and *Chandra* ACIS-I observations are indicated by solid and dashed boxes, respectively.

magnitudes JHK. The cross-match between the two catalogs was performed using the match service available at the CDS. By adopting a matching radius of 1″, we found that 431 860 of the 568 811 entries in our catalog have at least one counterpart in the 2MASS catalog.

The field we studied has been also included in the Vela-Carina *Spitzer* IRAC program, an extension program of the Galactic Legacy Infrared Midplane Survey Extraordinaire (GLIMPSE, Benjamin et al. 2003; Churchwell et al. 2009). We used the Vela-Carina Catalog (Zasowski et al. 2009), which in NW-VMR includes 170 206 objects with IRAC/*Spitzer* magnitudes. We cross-matched the list of IRAC sources with our catalog by adopting a matching radius of 0.″5 and found that 89 263 IRAC sources have a counterpart in our optical catalog[3].

In addition, we used the TGAS subset of the *Gaia* DR1 catalog (Gaia Collaboration 2016a, 2016b), limited to the objects included in the Hipparcos and *Tycho*-2 catalogs, for which we have positions, proper motions (PM), and parallaxes. The TGAS catalog was cross-matched[4] with the APASS catalog in NW-VMR, finding 3 065 matches within 1″.

In NW-VMR, several X-ray sources were also found from the ROSAT High Resolution Imager (HRI, 1RXH, third Release) and from the *Chandra* ACIS observations taken from the *Chandra* Data Archive (Wang et al. 2016). The field of view (FOV) of these observations are shown in Fig. 1. We cross-matched the two X-ray catalogs, including 25 *Chandra* and 75 ROSAT sources (with 3 sources in common to the two catalogs), with our optical catalog using the match service provided by the CDS, and adopting a radius of 5″. Within the NW-VMR area considered here, we considered the optical counterparts closest to the 97 X-ray sources as YSOs.

In particular, we have 8 and 34 X-ray sources from the ROSAT catalog that fall in RCW 33 and RCW 32, respectively and 40 X-ray sources in RCW 27, 36 of which are from the ROSAT catalog and 7 from the *Chandra* ACIS catalog, with 3 objects detected with both *Chandra* and ROSAT. The very small number of X-ray detections is due to the limited ROSAT sensitivity and to the short exposure times (from 1 to 46 ks) and coverage of the *Chandra* observations in this region.

3. Candidate young stars with ongoing accretion from *Hα* excesses

CTTS stars are YSOs with ages younger than few Myr, characterized by a circumstellar disk that transfers its matter onto the central star. This process involves high velocities of the gas that impacts on the star with a subsequent formation of a surface shock emitting predominantly in the UV, while Hα emission is produced in the accretion funnel. The first gives rise to the UV flux excess distinctive of CTTS, while the second can be photometrically detected through the $(r - H\alpha)$ color, which is a measurement of the strength of the Hα emission line relative to the photospheric continuum in the r band.

Figure 2 shows the $r - H\alpha$ versus $r-i$ color-color diagram (CCD), for all 473 998 VPHAS+ objects in the NW-VMR region with color errors <0.1 mag. The synthetic unreddened main sequence for stars with spectral type from O6V to M2V and the giant locus for stars with spectral type from K0III to M5III, computed by Drew et al. (2014), are also shown. Since the NW-VMR region includes a very large area with patterns of dark obscuring matter, spatially variable reddening is expected. This explains the large spread in colors around the synthetic loci. Neverthless, the

[3] The GLIMPSE point source accuracy is typically 0.3 arcsec.
[4] Using the match service provided by CDS.

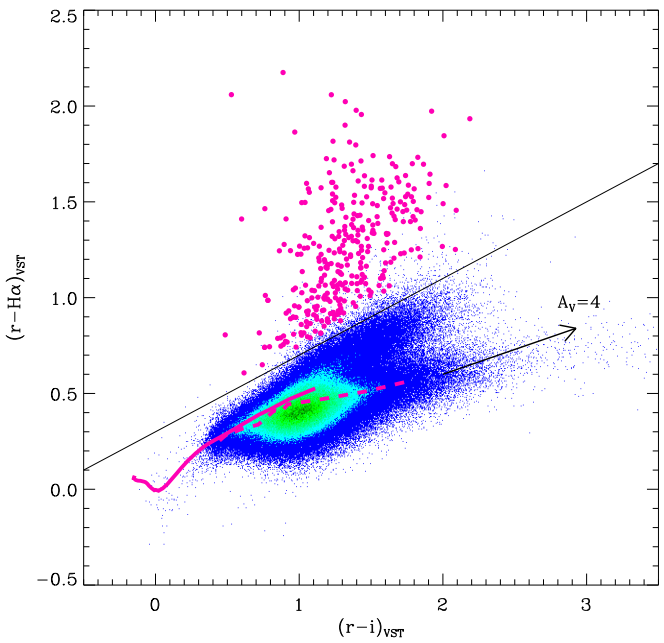

Fig. 2. VST $r-\mathrm{H}\alpha$ vs. $r-i$ diagram plotted as a two-dimensional stellar-density histogram using a binning of 0.005×0.005 and an eight-level color-coded scale such that high source densities (130 per bin) are dark green and the lowest densities (one per bin) are violet. The magenta solid and dashed lines are the synthetic unreddened main sequence and giant loci, respectively, given by Drew et al. (2014), and the black solid line is the limit adopted to select objects with Hα excesses, drawn as magenta circles.

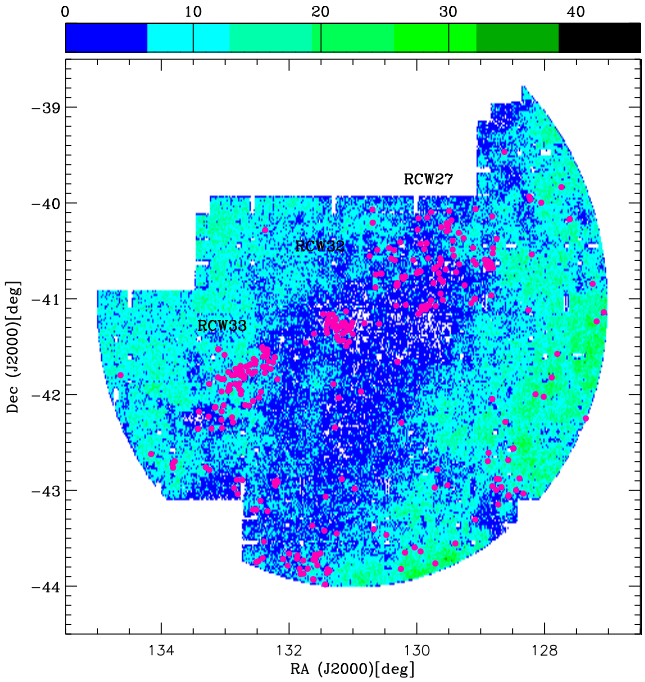

Fig. 3. Spatial distribution of the VPHAS+ stars in the NW-VMR region, plotted as a two-dimensional stellar-density histogram using a binning of $0\overset{\circ}{.}02\times0\overset{\circ}{.}02$ and a seven-level color-coded scale such that high source densities (45 per bin) are dark green and the lowest densities (one per bin) are blue. Objects with Hα excesses are drawn as magenta circles.

bulk of main sequence and giant stars is enclosed within the blue region, while objects with larger $r-\mathrm{H}\alpha$ are stars with Hα emission lines. We thus consider as stars with Hα excesses those with $r-\mathrm{H}\alpha$ color higher (with at least 5σ confidence) than the limit $r-H\alpha = 0.3+0.4\times(r-i)$. In this way, we select 329 CTTS candidates.

Figure 3 shows the spatial distribution of VPHAS+ objects in the NW-VMR region. Even though not the whole region is covered by VPHAS+ observations, the three H II regions we study are completely covered, except for the northern part of RCW 27. The 329 objects selected as Hα emission line stars are overplotted and clearly show a peculiar pattern with a tight concentration in RCW 32, a round but quite sparse distribution in RCW 27, and an elongated concentration in the RCW 33 region. This distribution is very similar to that found for the Hα-emitting stars by Pettersson & Reipurth (1994).

In order to understand the nature of the selected objects, we plot them in the r versus $r-i$ diagram shown in Fig. 4. Most of the selected objects are on the red side of the diagram and are consistent with a low-mass population of PMS stars, with ages younger than 10 Myr, as derived from the comparison with the PISA 10 Myr isochrone (Tognelli et al. 2011; Randich et al. 2018), assuming a distance of 750 pc and reddening $E(B-V)=0.2$ (see Sect. 5). These results strongly suggest the presence of three young clusters with different spatial distributions associated to the H II regions RCW 33, RCW 32, and RCW 27, respectively.

4. Candidate disk-bearing young stars from NIR excesses

Near-infrared excesses with respect to photospheric stellar colors are a very efficient tool for selecting YSOs. Several optical/NIR colors can be used to select objects with evident NIR excesses due to the presence of a circumstellar dusty disk in YSOs. *Spitzer*/IRAC CCDs are a powerful method for distinguishing YSOs with disk from old stars, since IR excesses in these colors do not follow the reddening direction and can therefore easily be separated from reddened objects. The [3.6]–[4.5] vs. [5.8]–[8.0] diagram in Fig. 5 includes all the objects with errors smaller than 0.2 mag and with $S/N>10$ in all four bands, as done in Zasowski et al. (2009) for data from the same survey. Using the conditions given in Gutermuth et al. (2009), which involve all IRAC/*Spitzer* magnitudes, we selected 461 candidate Class II, that is, disk-bearing objects, and 20 Class I YSOs, that is, YSOs still surrounded by the infalling material from which they form.

We also searched for possible contaminants (AGN or PAH galaxies) by following the definitions given in Gutermuth et al. (2009). We found that our sample of Class II YSOs includes 15 sources that are likely PAH contaminants, and we removed them from our sample.

Warm disks can show IR excesses in the K and H bands, but also in the J band, and the $J-H$ versus $H-K$ diagram is usually considered to select Class II stars (Meyer et al. 1997; Cieza et al. 2005). However, in this diagram it is very difficult to distinguish reddened objects from NIR excesses, since the region consistent with Class II stars overlaps with that of reddened objects, and therefore only objects with very strong NIR excesses can be selected from this diagram. Conversely, objects with excesses in the H or K bands can be very well distinguished from reddened objects if the diagram involves an optical color, dominated by photospheric emission even in Class II stars. For example, as discussed in Damiani et al. (2017), in the $r-i$ versus $J-H$ and/or $r-i$ versus $H-K$ diagrams, objects with excesses in the $H-K$ or $J-H$ colors can be confidently found on the red side of the main locus of normal reddened stars.

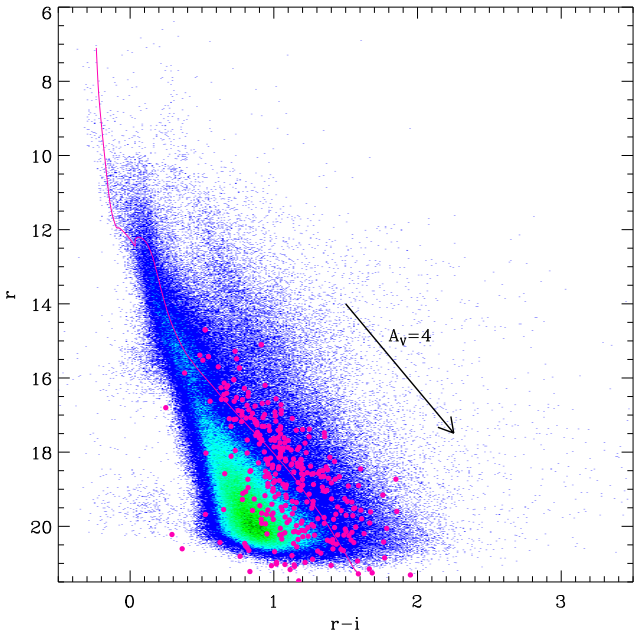

Fig. 4. SDSS r vs. $r-i$ diagram plotted as a two-dimensional stellar-density histogram using a binning of 0.01×0.01 and a 7 level color-coded scale such that high source densities (70 per bin) are dark-green and the lowest densities (one per bin) are blue. The magenta solid line is the 10 Myr PISA isochrone, assuming a distance of 750 pc and $E(B-V) = 0.2$. Objects with Hα excesses are drawn as magenta circles.

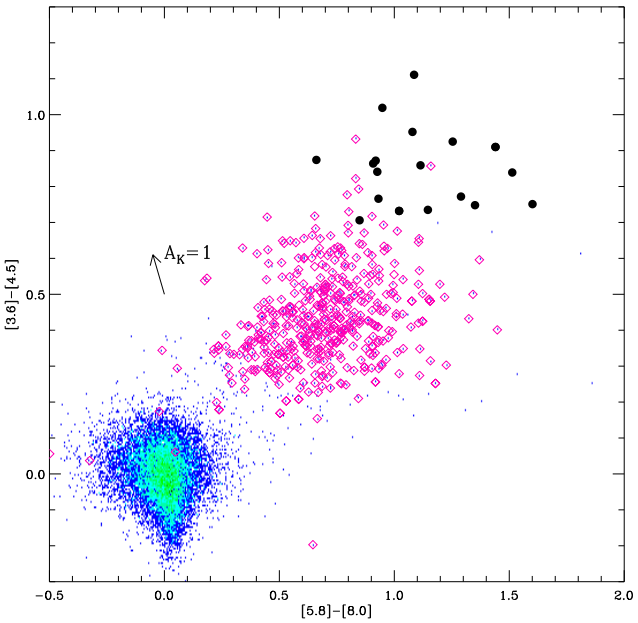

Fig. 5. [3.6]−[4.5] vs. [5.8]−[8.0] diagram plotted as a two-dimensional stellar-density histogram using a binning of 0.01×0.01 and a seven-level color-coded scale such that high source densities (29 per bin) are dark green and the lowest densities (one per bin) are blue. Class II stars are drawn as magenta diamonds, and Class I objects are indicated by black points. The reddening vector for $A_K = 1$ based on the extinction law in the direction of RCW 49 of Indebetouw et al. (2005) is shown as a filled arrow.

Figures 6–8 show the $r-i$ versus $H-K$, the $r-i$ versus $J-H$, and the $J-H$ versus $H-K$ diagrams of all objects with errors in $r-i$, $H-K$, and $J-H$ smaller than 0.1. It is evident that the bulk of the objects, mostly including giants and MS stars, follows the reddening vector. In this work we adopted the relations of the extinction curve with $R_V = 3.1$ given in Table 1.

The comparison of the data with the 10 and 100 Myr isochrones suggests that the tail of objects in Fig. 7 with $J-H$ around 0.6 and $r-i \gtrsim 1$ is the locus of M-type stars, while objects on the right of the dashed lines in the first two diagrams can be considered candidate YSOs. In total, 221 YSOs show excesses in both the $J-H$ and $H-K$ colors. Of these, 111 were selected as YSOs with a disk also using the IRAC data, while the remaining 110 lie outside the region covered by the IRAC/*Spitzer* observations. This finding is fully consistent with the observation coverage.

To also include the objects that lack detections in the less sensitive 5.8 and 8.0 μm bands, or with low excess in the J band, we selected 296 additional YSOs by taking objects with excess in the $H-K$ color that fulfill at least one of the previous three conditions involving the IRAC colors [3.6]–[4.5], [3.6]–[5.8], and [4.5]–[8.0]. Finally, to include possible YSOs with a low excess in the K band, we selected another 125 YSOs with excess in $J-H$ and in at least one of the IRAC colors. We finally assembled a total of 559 Class II YSOs that are included in at least one of the samples selected as described above, plus 20 Class I YSOs that are shown in Fig. 9, where the area covered by IRAC/*Spitzer* observations is also shown. The spatial distribution of the Class II and I stars is very similar to that found in the previous section for CTTS, and it again confirms the presence of three embedded young clusters in NW-VMR. The circular boundaries shown in the figure trace the locations of the dusty shells or bubbles that surround the three H II regions, as is shown in the WISE image of the region (see Fig. 22).

Table 1. Relations for a G2V star using the Cardelli et al. (1989) and O'Donnell (1994) extinction curve with $R_V = 3.1$ in the SDSS ugriz and 2MASS photometric systems (Marigo et al. 2017).

$\frac{A(u)}{A(V)}$	$\frac{A(g)}{A(V)}$	$\frac{A(r)}{A(V)}$	$\frac{A(i)}{A(V)}$	$\frac{A(z)}{A(V)}$	$\frac{A(J)}{A(V)}$	$\frac{A(H)}{A(V)}$	$\frac{A(Ks)}{A(V)}$
1.569	1.206	0.871	0.683	0.492	0.294	0.181	0.118

5. Kinematic populations

5.1. Trumpler 10 association

Even if limited to very bright stars, *Gaia* TGAS data give us the opportunity to study the kinematics across large fields. In order to understand whether the three young populations belong to the same molecular cloud and share a similar motion, we compared their PMs and parallaxes. As has been described in the literature, the VMR is behind the intermediate-age OB association Trumpler 10 (RA = 131°.872, Dec = −42°.40), of which 23 members, 22 B-type and 1 A0V star are known (de Zeeuw et al. 1999; Kharchenko et al. 2013).

The distance of Trumpler 10 has been estimated by several authors to be 417 pc (Kharchenko et al. 2013), 424 pc (Dias et al. 2002), and 366 ± 23 pc (de Zeeuw et al. 1999). Located at a galactocentric distance of $R_{GC} = 8.1$ kpc, it shows a relatively low reddening, $E(B-V) = 0.029$ (Kharchenko et al. 2013). The most recent values for the cluster age are 24 Myr (Kharchenko et al. 2013), ~35 Myr (Dias et al. 2002), and 15 Myr (de Zeeuw et al. 1999).

Since our field includes this association, we first studied the PM and parallax distributions around its center, as shown in Fig. 10. To detect a population sharing the same motion and a common parallax, we adopted the following procedure: we computed the

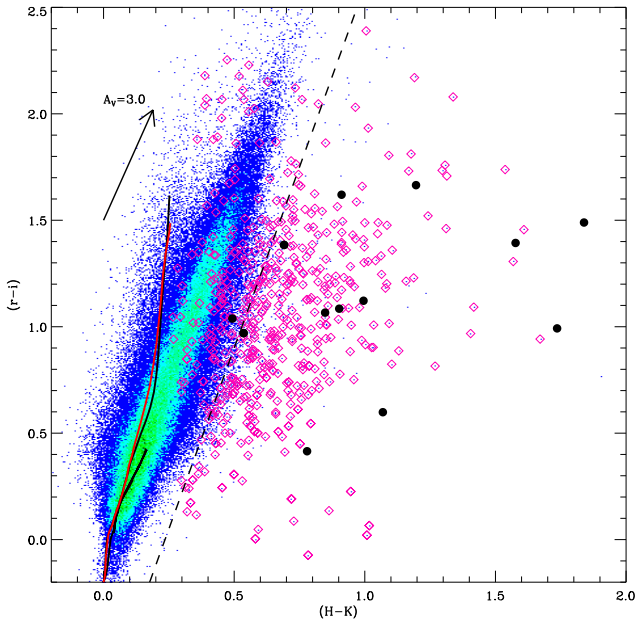

Fig. 6. $r-i$ vs. $H-K$ diagram plotted as a two-dimensional stellar-density histogram using a binning of 0.01×0.01 and a seven-level color-coded scale such that high source densities (54 per bin) are dark green and the lowest densities (one per bin) are blue. The symbols are the same as in Fig. 5. The black and red solid lines are the 100 and 10 Myr PISA isochrones. The reddening vector is also shown.

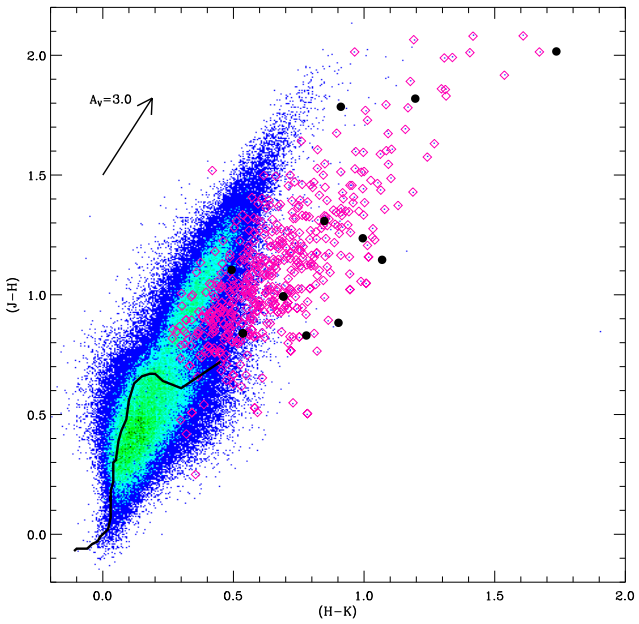

Fig. 8. $J-H$ vs. $H-K$ diagram plotted as a two-dimensional stellar-density histogram using a binning of 0.01×0.01 and a seven-level color-coded scale such that high source densities (56 per bin) are dark green and the lowest densities (one per bin) are blue. The symbols are the same as in Fig. 5. The black solid line shows the MS locus (Kenyon & Hartmann 1995).

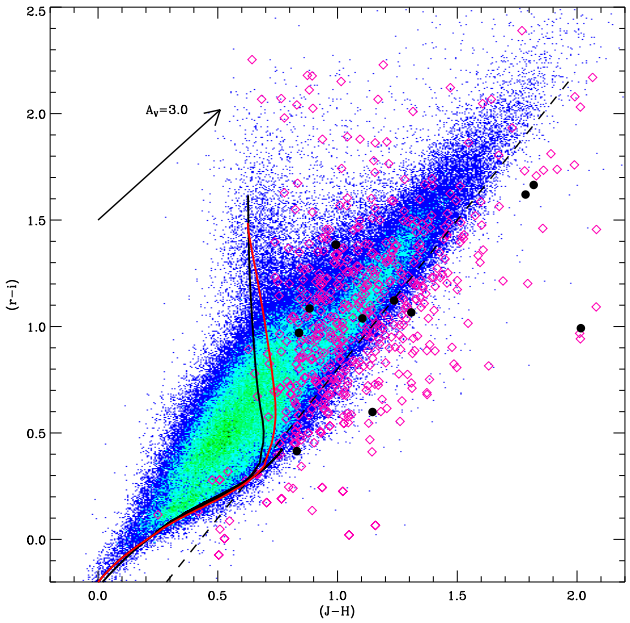

Fig. 7. $r-i$ vs. $J-H$ diagram plotted as a two-dimensional stellar-density histogram using a binning of 0.01×0.01 and a seven-level color-coded scale such that high source densities (39 per bin) are dark green and the lowest densities (one per bin) are blue. The symbols are the same as in Fig. 5.

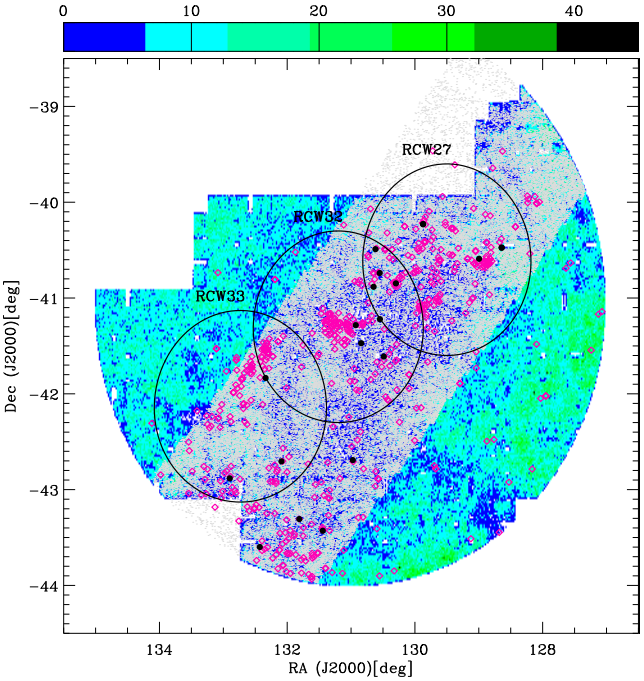

Fig. 9. Spatial distribution as in Fig. 3, where all the *Spitzer*/IRAC sources are overplotted with gray symbols. YOSs with IR excesses are indicated as in Fig. 5. The three circular boundaries delimit the regions of the three clusters.

maximum of a bidimensional array of PMs in RA and Dec, assuming a PM bin of 1 mas yr^{-1} both in μ_α and μ_δ in the range $-20 < \mu_\alpha/\mathrm{mas\ yr^{-1}} < 20$ and $-20 < \mu_\delta/\mathrm{mas\ yr^{-1}} < 20$ and in parallax steps of $\Delta\pi = 1$ mas. This large π step was chosen to account for the large errors on the parallax values of the TGAS *Gaia* data. To avoid a binning dependence, we repeated the computation by shifting by 0.1 mas the parallax bin while exploring the parallax range $0 < \pi/\mathrm{mas} < 4$ (corresponding to distances larger than 250 pc), where most of the objects are distributed. The maximum value of each array represents the tridimensional condition to detect clusters of objects at the same distance sharing the same

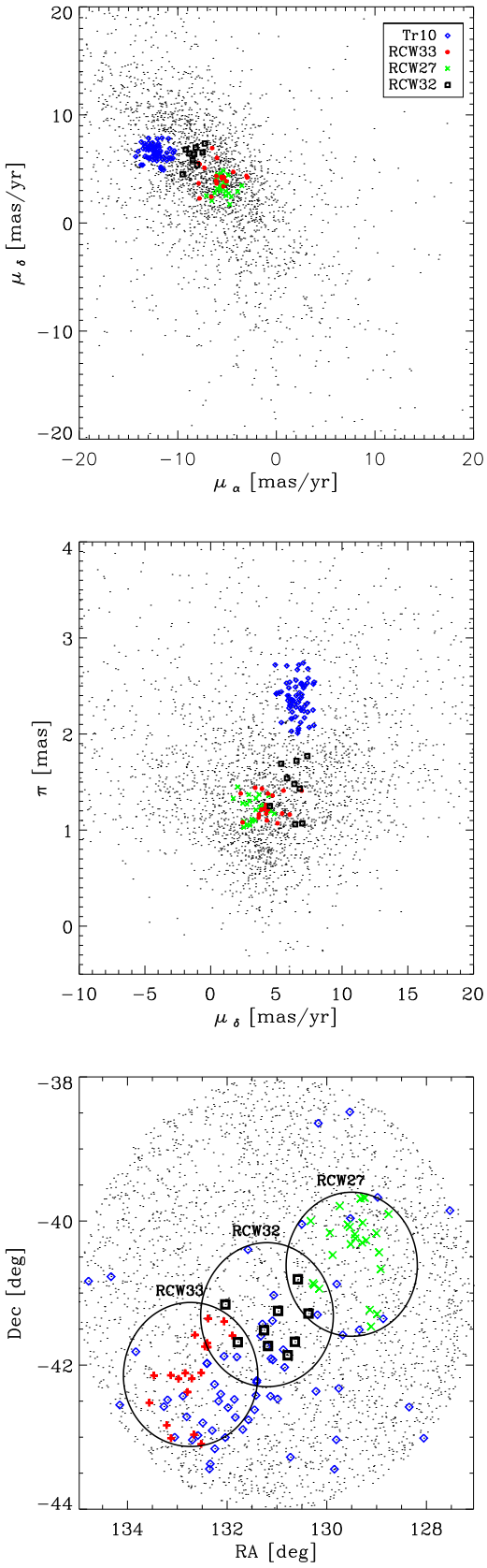

Fig. 10. μ_α vs. μ_δ (*upper panel*), π vs. μ_δ (*middle panel*) and spatial distribution (*lower panel*) of the TGAS catalog in the region of the VMR studied here. Blue diamonds are associated with the Trumpler 10 cluster, red pluses are associated with YSOs in the RCW 33 region, green crosses are associated with YSOs in the RCW 27 region, and black squares are associated with YSOs in the RCW 32 region.

motion. For each parallax bin, we considered the μ_α and μ_δ corresponding to the maximum of the array, and therefore we selected all the objects with $\sqrt{(\mu_\alpha)^2 + (\mu_\delta)^2} < 2$ mas. If the number of objects within this tridimensional region is larger than 10, then the corresponding μ_α, μ_δ, and π are associated with a population[5]. As expected, we obtained similar values for close parallax ranges, and therefore we considered the median values associated with the selected maxima as the final parameters for a population.

To detect the population of Trumpler 10, we considered the whole TGAS catalog in the entire region we studied because this association is known to be highly dispersed on the sky. In this region, our procedure enabled us to detect a main population at $\pi = 2.37$ mas, corresponding to 422 ± 32 pc (1σ uncertainty). We conclude that this latter population is the one associated with Trumpler 10, and it includes 63 objects.

Figure 10 also shows the spatial distribution of the TGAS stars found in this region, where the population of Trumpler 10 (blue symbols) is clearly distinct from the others (see below) for its kinematic parameters, while its spatial distribution is highly dispersed throughout the region, confirming the results of de Zeeuw et al. (1999). The color-magnitude diagram (CMD) of these objects is shown in Fig. 11 and is compared with the PISA isochrone with the parameters indicated in the figure. The sequence shows a spread around the isochrone. A thorough assessment of the nature of this spread, which would require detailed investigation of the entire population of the association, is beyond the aim of this work.

5.2. Cluster Cr 197 and RCW 32

The analysis of PMs and parallaxes in the region of RCW 32, corresponding to the cluster Cr 197, has been performed in the same way as for Trumpler 10. This last association is spread across a large region overlapping that of Cr 197. For the kinematic analysis of Cr 197, we used only the TGAS data within a radius of 45′ from its center. This radius has been chosen to avoid the two neighboring regions RCW 33 and RCW 27, which show a more dispersed spatial distribution. In addition, we discarded objects with $\mu_\alpha < -10$ mas yr^{-1} and $\pi > 2$ mas, since they are associated with Trumpler 10. Our procedure enabled us to detect two groups of objects in the PM plane that lie in the same parallax range. The two populations do not show a peculiar spatial distribution, being both quite sparsely distributed, but their distribution in the CMD suggests that the group of objects corresponding to $(\mu_\alpha, \mu_\delta) = (-8.3, 5.8)$ mas yr^{-1} in the parallax range $1.0 < \pi < 2.0$ (indicated with black squares in Fig. 10) can be associated with the cluster Cr 197. The mean parallax of these objects is 1.44 mas, which corresponds to a distance of 692 ± 128 pc. The nine selected objects (black squares in Figs. 10 and 11) follow the 10 Myr PISA isochrone at a distance of 692 ± 80 pc ($\pi = 1.45$) quite well, assuming $E(B-V) = 0.02$, as shown in Fig. 11. Our analysis therefore suggests a cluster distance significantly smaller than that found by Bonatto & Bica (2010), namely 1050 ± 200 pc, based on NIR photometry and a statistical field star decontamination. Our value is, instead, consistent with the distance of $\simeq$700 pc derived by Georgelin et al. (1973) and Crampton & Fisher (1974). In addition, the r versus $r-i$ diagram suggests that the cluster is less reddened than the value reported in the literature, equal to $E(B-V) = 0.34$ (Bonatto & Bica 2010).

[5] The adopted threshold corresponds to about 3σ of the distribution of objects where no hint of clustering is found.

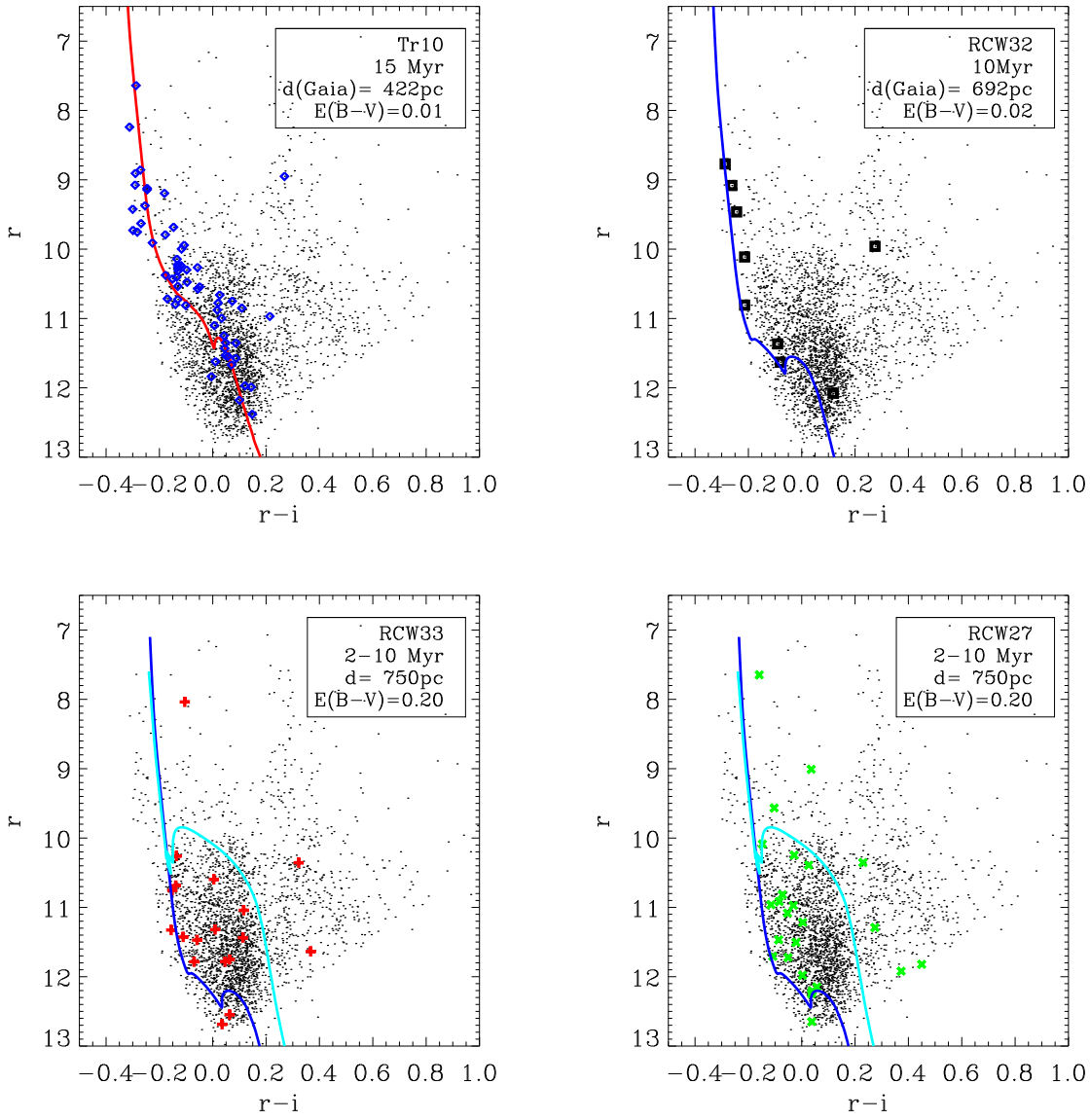

Fig. 11. *r* vs. *r*−*i* diagrams of the cluster Trumpler 10 and of the three regions centered on RCW 33, RCW 27, and RCW 32. The colored symbols are the same as in Fig. 10 and indicate the candidate members for each region, selected kinematically using *Gaia* data.

5.3. Cluster Vela T2 and RCW 33

As in the previous sections, we performed the PM and parallax analysis also in the RCW 33 region. Even in this case, there is a strong contamination from the Trumpler 10 members, and therefore we discarded objects with $\mu_\alpha < -10$ mas yr^{-1} and $\pi > 2$ mas. After this, the diagram (μ_α, μ_δ) shows a group of objects with a quite elongated distribution in the μ_α axis. This includes two groups that are distinguishable in the parallax diagram, in the range $0.5 < \pi/\mathrm{mas} < 1.0$ and $1.0 < \pi/\mathrm{mas} < 1.5$. The second subgroup, corresponding to a distance of about 800 pc, is centered on $(\mu_\alpha, \mu_\delta) = (-5.57, 4.10)$ mas yr^{-1} (red symbols in Figs. 10 and 11). This population includes 19 objects with an elongated spatial distribution similar to the YSOs selected above. In the CMD, these objects lie in a region compatible with both MS and PMS stars (Fig. 11). We associate this group of stars with the cluster Vela T2.

5.4. Cluster Vela T1 and RCW 27

The PM analysis of the objects in RCW 27 shows a clearly distinct clump in the (μ_α, μ_δ) diagram for $\pi > 1.0$ mas at $(\mu_\alpha, \mu_\delta) = (-5.48, 3.39)$ mas yr^{-1}. The population, corresponding to RCW 27, was selected by taking objects with PMs within 2 mas yr^{-1} from this peak and with $1.0 < \pi < 1.5$ mas. This population includes 25 objects that mainly lie in the northwestern part of RCW 27 (green symbols in Figs. 10 and 11). The CMD of the selected objects is consistent with a PMS population located at about 750 pc, with ages younger than 10 Myr.

6. Summary of the classical YSO selection

We summarize here the properties of candidate YSOs found in the NW-VMR including all the objects with Hα or NIR excesses, selected as described in Sects. 3 and 4, with an X-ray detection, or with PMs and parallaxes consistent with the populations in RCW 33, RCW 32, or RCW 27, selected as described in Sect. 5.

We selected a total of 907 candidate YSOs in the whole area. Included in the circular regions with radius 1 deg in RCW 33, RCW 32, and RCW 27 are 210, 177, and 288 candidates, respectively. We note that the YSOs falling in the overlapping

Table 2. Optical/NIR photometry and membership criteria of YSOs selected with classical methods.

CNAME	RA (J2000)	Dec (J2000)	*u*	*g*	*r*	*i*	*Hα*	*J*	*H*	*K*	M1	M2	M3	M4
08442605-4105159	131.10853	−41.08775	...	...	11.43	11.22	...	10.19	9.80	9.69	0	0	0	1
08435467-4114538	130.97779	−41.24827	...	...	9.46	9.71	...	9.33	9.35	9.30	0	0	1	0
08441101-4116189	131.04588	−41.27192	...	...	11.65	11.20	...	10.22	...	...	0	0	0	1
08443774-4115371	131.15724	−41.26032	...	...	14.75	14.11	...	...	...	...	0	0	0	1
08444029-4116378	131.16788	−41.27716	...	...	7.24	7.23	...	6.39	6.25	6.24	0	0	0	1
08451790-4112462	131.32456	−41.21283	...	...	14.90	14.27	...	...	...	...	0	0	0	1
08444546-4117322	131.18942	−41.29228	...	...	14.57	13.94	...	...	...	...	0	0	0	1
08451500-4117349	131.31251	−41.29301	...	...	12.19	12.05	...	11.20	10.93	10.87	0	0	0	1
08445256-4124287	131.21902	−41.40797	...	...	8.78	8.71	...	7.83	7.55	7.48	0	0	0	1
08411684-4050026	130.32015	−40.83406	...	...	11.22	11.09	...	10.11	9.69	9.37	0	1	0	0
08450201-4130582	131.25836	−41.51617	...	...	8.77	9.06	...	8.80	8.82	8.88	0	0	1	0

Notes. M1, M2, M3, and M4 stand for membership from Hα, IR excesses, kinematics and X-ray detection, respectively; 1 indicates member while 0 indicates non-member. The full table is available at the CDS.

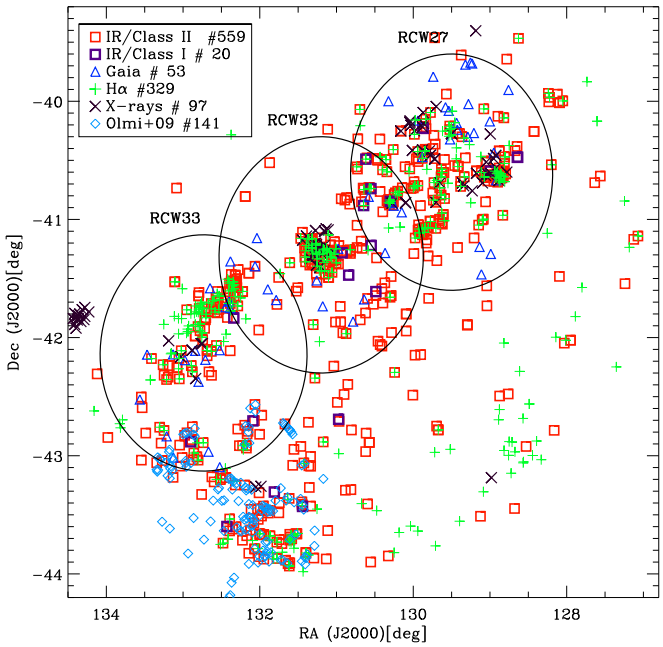

Fig. 12. Spatial distribution of all candidate YSOs, selected with different membership classical criteria, plotted with different symbols. Cyan diamonds show the 141 submillimeter cores found with the BLAST survey by Olmi et al. (2009). The three circles of 1′in radius delimit the regions around the three clusters.

areas were associated with the external areas, that is, RCW 33 and RCW 27. We refer to these 907 objects as members selected with classical methods. The optical/NIR photometry and the membership information of the selected YSOs are given in Table 2.

We note that the list is not complete since the spatial coverage of data used to select them is incomplete. The spatial distribution of all the objects selected as YSOs is shown in Fig. 12. We omitted from Fig. 12 the 63 kinematic objects that are candidate members of Trumpler 10 since they are not related to the young populations we investigate here.

As discussed above, many of the selected YSOs define three young clusters associated with the three H II regions. However, an additional stellar subcluster is located immediately to the south of RCW 33, corresponding to Vela-D. It is composed of mainly Hα and IR-excess YSO candidates. This region has been the subject of a Balloon-borne Large-Aperture Submillimeter Telescope (BLAST) survey by Olmi et al. (2009), where 141 pre-stellar and protostellar sources have been found. The presence of YSOs detected also in the optical and NIR bands and the strong spatial correlation of these YSOs with the cores found in Olmi et al. (2009) is further confirmation of the ongoing star formation in this region, which is characterized by the lack of massive O-type stars.

We note that an additional group of X-ray sources is located to the east of RCW 33. These objects are located in a region devoid of YSOs selected in this work that lies at the boundary of the field, and thus we are not able to assert whether this group of objects is associated with a young subcluster.

The three circular areas in the H II regions have the best coverage, but the northern region of RCW 27, for example, lacks VPHAS+ data and the northern regions of RCW 33 and RCW 32 lack *Spitzer*/IRAC data. For this reason, we avoid any analysis requiring completeness of the samples. We found 136 YSOs with evidence of accretion from Hα and of a circumstellar disk from the IR. Three objects have NIR excess, selected also with PMs and parallax, while no objects, selected kinematically, show evidence of accretion or X-ray emission. Most of the candidate YSOs have only one youth indicator, and this suggests that the methods are complementary.

We find that members selected as YSOs with NIR, Hα excess, and X-rays show a similar spatial distribution in each of the three H II regions, even though the X-ray sample is very limited in both spatial coverage and duration of observations. The members selected using *Gaia* data, expected to be the more massive ones, show a spatial distribution similar to that of the other members in Vela T2 and T1, while in Cr 197, they are poorly correlated with the other member positions. This could be due to the lower performance of *Gaia* data in very crowded regions, such as the cluster Cr 197 in RCW 32, or it might be due to source extinction. The TGAS sample mainly includes lightly absorbed stars. Since the region harbors a large number of spatially clustered disk-bearing YSOs, clouds, and a nebular background, a spatially varying source extinction is expected, which could explain the poor correlation with *Gaia* members.

In conclusion, we find that the whole region includes different sites of ongoing or recent SF. We concentrate our attention on the three areas of the H II regions, whose properties we study in the following sections.

7. Features of M-type stars

The region studied in this work lies on the galactic plane and therefore includes a large number of field stars. Because of the molecular clouds, the background objects are expected to be very reddened, while those in front of the nebula are likely affected by low reddening. In general, in the optical and NIR CCD and CMD, foreground and background field stars cannot be distinguished from YSOs, since the color distribution of all these objects follows the direction of the reddening vector. Nevertheless, using appropriate combinations of optical and NIR magnitudes, the color distribution of M-type stars does not follow the reddening vector, and this property can be used to select M-type stars, as recently discussed in Damiani (2018) and Venuti (in prep.).

This is clearly visible in the $r-i$ versus $i-J$, $i-H$, and $i-K$ diagrams shown in Fig. 13, where the comparison with the theoretical loci of PMS, MS, and giant stars shows that the region of M-type stars ($r-i \gtrsim 0.75$) is clearly distinguishable from that of hotter, reddened stars. In particular, the bulk of our data in the M-type range is compatible with stars affected by very low reddening, while all objects on the red side of the diagram are very reddened stars.

Following the position of the theoretical loci in the three diagrams compared to the bulk of objects that lie along the reddening vectors, we select as M-type stars all the objects with $r-i$ larger than the limits indicated by the solid green lines in all the three diagrams, and with $i - K > 2.2$. The simultaneous use of the three diagrams allows us to select a sample of M-type stars that is as clean as possible. In the three diagrams, YSOs selected with classical methods mainly lie in the region of reddened stars, and only a small fraction of them fall in the region of M-type stars. As expected, the spread of the selected YSOs in the $r-i$ versus $i-K$ diagram is larger than that in the $r-i$ versus $i-J$ diagram, since this sample includes stars with IR excesses, mainly in the K band. Therefore, it could include also M-type stars with disk or accretion, that, due to the presence of IR excesses, fall outside of the region of M-type stars.

A further feature of the M-type stars is that in the $r-i$ versus $i-J$ diagram the theoretical loci of PMS, MS, and giant stars almost overlap, while in the $r-i$ versus $i-H$ and $r-i$ versus $i-K$ diagrams they are quite separated. This occurs because the $i-H$ and $i-K$ colors of giant M stars of a given temperature are redder than those of MS stars, as is clearly evident in Fig. 14, where the stellar gravities for a set of theoretical PISA isochrones at solar metallicity are shown as a function of the $i-J$ and $i-K$ colors. This feature implies that the $i-H$ and $i-K$ colors of the PMS isochrones of ages $\gtrsim$10 Myr are similar to MS star colors, while for the very young PMS stars (0.5 Myr in the case of our models), the $i-H$ and $i-K$ colors are more similar to those of the giant locus, as shown in Fig. 15.

In the $r-i$ versus $i-H$ and $i-K$ diagrams, PMS isochrones with ages from 0.5 to 5 Myr are located between the giant and the MS loci. Therefore the PISA models predict that the $i-H$ and $i-K$ colors are sensitive to the stellar ages and gravities, at least for Log $g > 3.0$. The $i-H$ and $i-K$ colors of M-type giants, which are very low gravity objects (Log $g < 3.0$), are more similar to those of YSOs (<1 Myr) rather than to objects with ages >5−10 Myr. Within the limits of the photometric errors, at a given temperature (or analogously at a given $r-i$ color), the $i-H$ and $i-K$ colors can therefore be exploited to also constrain the luminosity class of M-type stars, as described below.

For each individual M star,we computed a reddening value from each of the three $r-i$ versus $i-J$, $i-H$, and $i-K$ diagrams by projecting back the observed colors along the corresponding

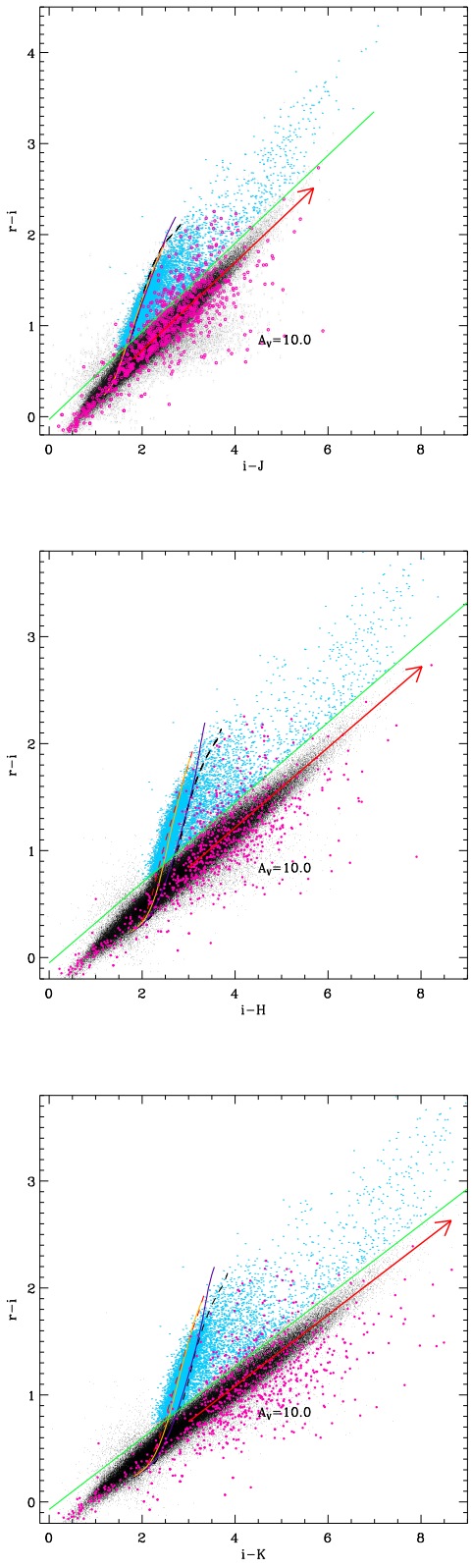

Fig. 13. $r-i$ vs. $i-J$, $i-H$, and $i-K$ diagrams plotted as a two-dimensional stellar density histogram on a gray scale, compared with the MS locus (dashed red line), the 10 Myr and 0.5 Myr isochrones (orange and purple lines), and the giant locus (black line) predicted by PISA models. YSOs selected with classical methods and objects selected as M-type stars are indicated with magenta and cyan symbols, respectively. The reddening vectors and the limits used for the selection of M-type stars are indicated as red arrows and green lines, respectively.

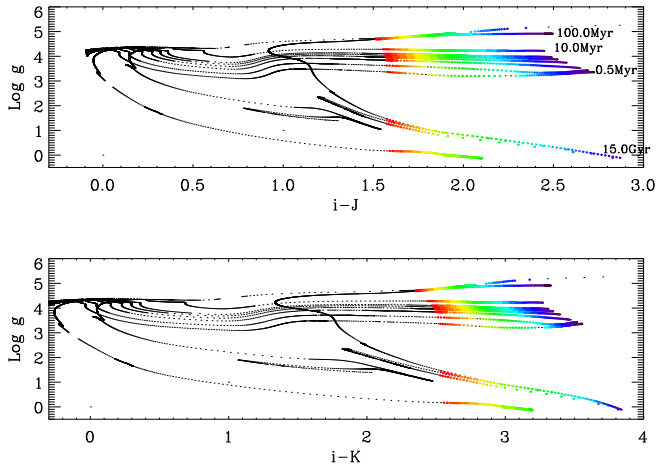

Fig. 14. Log g values vs. $i-J$ (*upper panel*) and $i-K$ colors (*bottom panel*) for a set of solar metallicity PISA isochrones with ages from 0.5 Myr to 15 Gyr. Different colors indicate different effective temperature values of M-type stars from 3000 K (violet lines) up to 4000 K (red lines) with a step of 50 k.

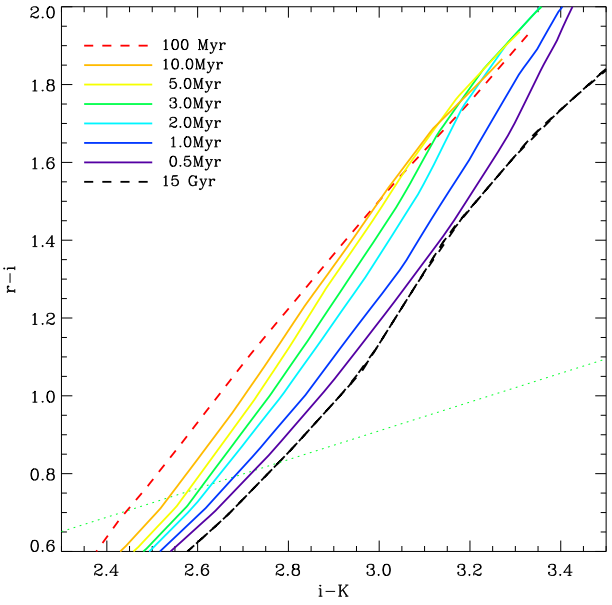

Fig. 15. Zoom of the $r-i$ vs. $i-K$ diagram showing isochrones of different ages. The dotted green line is the limit used to select M-type stars.

reddening vector onto one of the possible unreddened theoretical loci[6]. For the objects located blueward of the related model isochrone, we computed the A_V only when the color was bluer than the related model isochrone by less than the maximum photometric error, that is, 0.1414 mag. In these cases, the A_V is negative but compatible with $A_V = 0$.

As discussed before,in the $r-i$ versus $i-J$ diagram, the theoretical loci of giants, MS, and PMS stars almost overlap, and therefore the derived absorption values A_V will be almost independent of the gravity. In contrast, in the $r-i$ versus $i-H$ or $i-K$ diagrams, the derived A_V will depend on the gravity, since in these diagrams the loci are quite separated. For each star, we therefore derived the A_V sets $(A_V^J, A_V^H, A_V^K)_l$ from the three diagrams and each adopted evolutionary status l (with l = MS or G, indicating the loci of MS stars and giants, or PMS indicating any isochrone with age $\lesssim$10 Myr). For each given evolutionary status, we derived the means $\langle A_V\rangle_l$, that is, $\langle A_V\rangle_{MS}$, $\langle A_V\rangle_{PMS}$, and $\langle A_V\rangle_G$ and the standard deviations $\sigma(A_V)_l$, that is, $\sigma(A_V)_{MS}$, $\sigma(A_V)_{PMS}$, and $\sigma(A_V)_G$ from the three diagrams. For the case of the PMS state, the A_V calculation includes the multiple age-dependent sets of $(A_V^J, A_V^H$, and $A_V^K)$, corresponding to the isochrones of 0.5, 1.0, 2.0, 3.0, 5.0, and 10.0 Myr ages.

Clearly, the σ will be large if the adopted evolutionary stage is not the correct one. Thus, we defined the best A_V estimate of each star as the mean $\langle A_V\rangle_l$ corresponding to the minimum $\sigma(A_V)_l$.

7.1. Bright M-type population

Figure 16a shows the r versus $r-i$ diagram of the M-type stars. We note that they appear to be grouped into two distinct populations, separated by the dashed line shown in the diagram. We first considered the brightest group, to which we refer to as bright M-type (BM) population, and in particular, we examined the spatial distribution of this sample, that, as shown in the figure (panel b), does not show any significant clustering. From this distribution, we infer that these objects are not correlated with the young population studied above, but, on the contrary, they are consistent with field M-type MS or giant stars, homogeneously distributed over the region. In order to constrain the luminosity class of these objects, we consider the values of $\sigma(A_V)_{MS}$ and $\sigma(A_V)_G$ defined in the previous section. The results are shown in Fig. 16, where we show the scatter plots of dispersion versus average value for $\langle A_V\rangle_G$ and $\langle A_V\rangle_{MS}$ in panels c and d, respectively.

The $\sigma(A_V)_G$ data show a tail of outliers at high values (red squares). We estimated the statistical parameters of the $\sigma(A_V)_G$ distribution while minimizing the effect of outliers by computing the median and the pseudo-sigma as the difference between median and the 16^{th} percentile, corresponding to 1 σ of a Gaussian distribution (0.50−(0.68/2.0) = 0.16). The median of the distribution is 0.17 mag and the pseudo-sigma is 0.06 mag. In contrast, the median of the $\sigma(A_V)_{MS}$ is 0.35 and the pseudo-sigma of 0.13. The first conclusion is that the values obtained assuming the two models show very different shapes. The $\sigma(A_V)_G$ distribution of most of the objects (black points) shows a very narrow peak, while the $\sigma(A_V)_{MS}$ distribution is much larger. For most of the objects, $\sigma(A_V)_G \ll \sigma(A_V)_{MS}$. This allows us to deduce that for this sample i) the A_V values obtained in each of the CCD using the giant model are more accurate than those obtained using the model of MS stars; ii) by computing the mean of the three values associated with the giant model, we obtain not only more accurate, but also more precise photometric A_V values; iii) the very narrow peak of the $\sigma(A_V)_G$ distribution of these objects suggests that all of them are consistent with a population of giants rather than MS stars. This latter result is consistent with their position in the r vs. $r-i$ diagram, since it is more likely that very reddened and relatively bright objects like these are M-type giants rather than M-type MS stars.

Finally, we selected 76 objects with $\sigma(A_V)_G > 0.35$ (i.e., larger than 3 pseudo-σ from the median of the distribution) for which $\sigma(A_V)_{MS} < \sigma(A_V)_G$. For these objects, the quite large spread of the $\sigma(A_V)_{MS}$ values does definitely suggest that they are not MS stars.We suspect that the A_V estimates obtained for these objects might not be reliable because we used only solar metallicity models, which are not appropriate if they are M-type stars with non-solar metallicities. As a consequence, with the models adopted in this analysis, we are not able to classify these 76 objects.

In conclusion, from the statistical values, indicated in Fig. 16, we deduce that most of the bright M-type stars (551/627) are giants

[6] The reddening value is converted into absorption by following the relations given in Table 1.

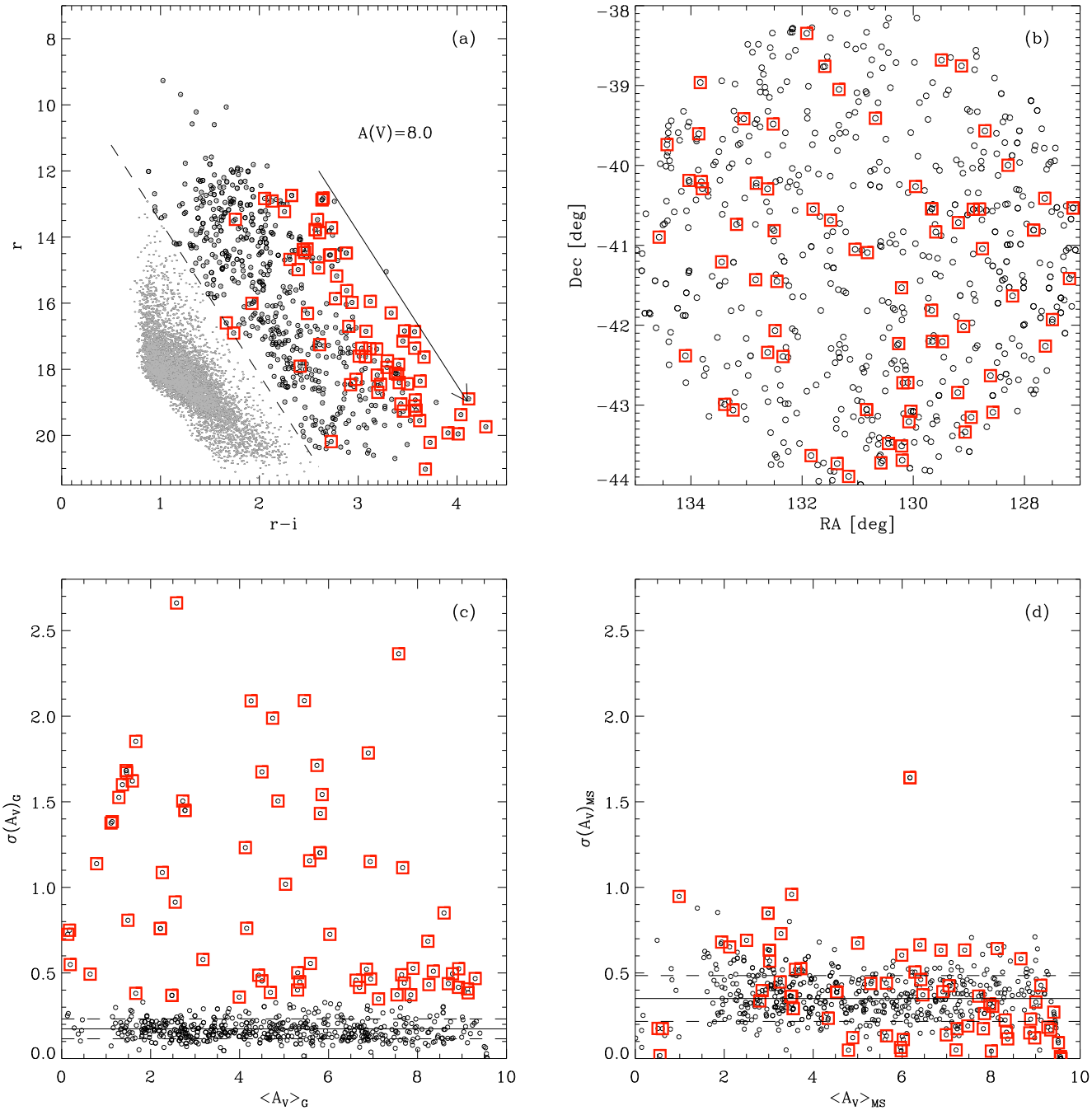

Fig. 16. *Panel a*: r vs. $r-i$ diagram of all the objects selected as M-type stars (gray symbols). Black dots show those whose r magnitude is brighter than the limit indicated by the dashed line, while red squares indicate the subsample including M-type for which the A_V values are not consistent with solar metallicity giants. The reddening vector is also indicated. Spatial distribution (*panel b*) and $\sigma(A_V)_l$ vs. the $\langle A_V \rangle_l$ values of bright M-stars, obtained assuming the giant locus (*panel c*) and the MS locus (*panel d*).The median and the median ± the pseudo-sigma are indicated by the solid and dashed lines, respectively, in *panels c and d*.

affected by absorption A_V ranging from ≃1.5 to 10, with an error on A_V of about 0.17 (corresponding to the median of the $\sigma(A_V)$ values).

7.2. Faint M-type population

The faint M-type (FM) population includes all objects selected as M-type stars with r magnitudes fainter than the limit indicated by the dashed line in panel (a) of Fig. 16, shown in the figure with gray symbols.

We expect this population to include field stars as well as YSOs belonging to the clusters we study here. We therefore computed for each star the triplets $(A_V^J, A_V^H, A_V^K)_{MS}$, $(A_V^J, A_V^H, A_V^K)_G$ and $(A_V^J, A_V^H, A_V^K)_{PMS(t)}$, with t indicating the isochrone ages 0.5, 1.0, 2.0, 3.0, 5.0, and 10.0 Myr.

As for the BM population, we computed the mean $\langle A_V \rangle_l$ and $\sigma(A_V)_l$ for each triplet. We also considered the best A_V estimate for a given star the $\langle A_V \rangle_l$ for which the $\sigma(A_V)_l$ is smallest.

This condition allows us to derive an A_V that is more accurate than the one obtained using only one diagram that could be

affected by the possible presence of circumstellar disk, with excesses in one or more of the three J, H, or K bands (Cieza et al. 2005). We note that if the M-type stars are affected by strong IR excesses, their colors are redder than the limit adopted to select M-type stars, and therefore they are not included in the sample of M-type stars. Nevertheless, young M-type stars with small IR excesses can fall in the region of M-type stars. In these cases, the A_V can be affected by the IR excesses and the $\sigma(A_V)$ could be larger than the one derived for disk-less M-type stars. These cases can be considered as candidate M-type young stars with a circumstellar disk.

7.2.1. Faint M-type MS stars

As described above, because the oldest PMS isochrones partially overlap the MS locus and the youngest ones with the giant locus, PMS stars can be misclassified as MS stars or giants and vice versa. In case of star forming regions, it is therefore not possible to definitively assign the age to the objects. Nevertheless, the best A_V values obtained with this method, within the uncertainties due to the photometric errors and the model accuracy, can be considered reliable to obtain intrinsic colors and magnitudes, since they do not depend on the knowledge of the stellar evolutionary stage, but only on the photometric indices.

Figure 17 shows the unreddened r_0 versus $(r-i)_0$ diagram, derived from the best A_V values for the faint M-type population, compared with the 0.5, 5.0, and 10.0 Myr and the 1 Gyr isochrones at the cluster distance. In this diagram, the only unknown parameter is the distance, but when we assume that the young population can be found only between the 0.5 and 10 Myr isochrone at the distance of 750 pc (see Sect. 5), we can conclude that all the objects with r_0 larger than the 10.0 Myr isochrone at the cluster distance (to which we added a delta r equal to 0.2 to take into account the errors) are not compatible with YSOs belonging to our clusters and therefore are expected to be field stars.Based on the position of the 1 Gyr isochrone, at the cluster distance, we deduce that they cannot be background M-type MS stars but are instead are compatible with foreground M-type MS stars with distance smaller than the cluster distance and approximately larger than about 300–400 pc. The 1 Gyr MS isochrone at 300 pc (400 pc) approximately corresponds to the late-M- (early-M) lower limit in r_0 that we adopted to delimit this sample of field stars. Our conclusion is confirmed by their spatial distribution, which is quite uniform, as expected for field foreground stars[7]. We refer to this population as the faint M-type MS (FM-MS) stars.

Figure 17 also shows the $\sigma(A_V)_{MS}$ values as a function of the $\langle A_V \rangle_{MS}$. As for the giants of the bright M-type population, we computed the median and pseudo-σ of the $\sigma(A_V)_{MS}$ values that are found to be 0.18, equal to that of bright giants, and 0.1, larger than the analogous value found for giants (0.06). The larger dispersion derived for MS stars may be due to the very low values of A_V ($\lesssim$0.8) found for most of these stars. In conclusion, we selected 1869 faint M-type objects that we classify as MS foreground field stars with distances between 300–400 and ~750 pc.

7.2.2. Faint M-type PMS stars

In the following, we analyze the faint M-type population in the PMS photometric region (FM-PMS), which is the region included between the 0.5 and 10 Myr isochrones at the cluster distance. As

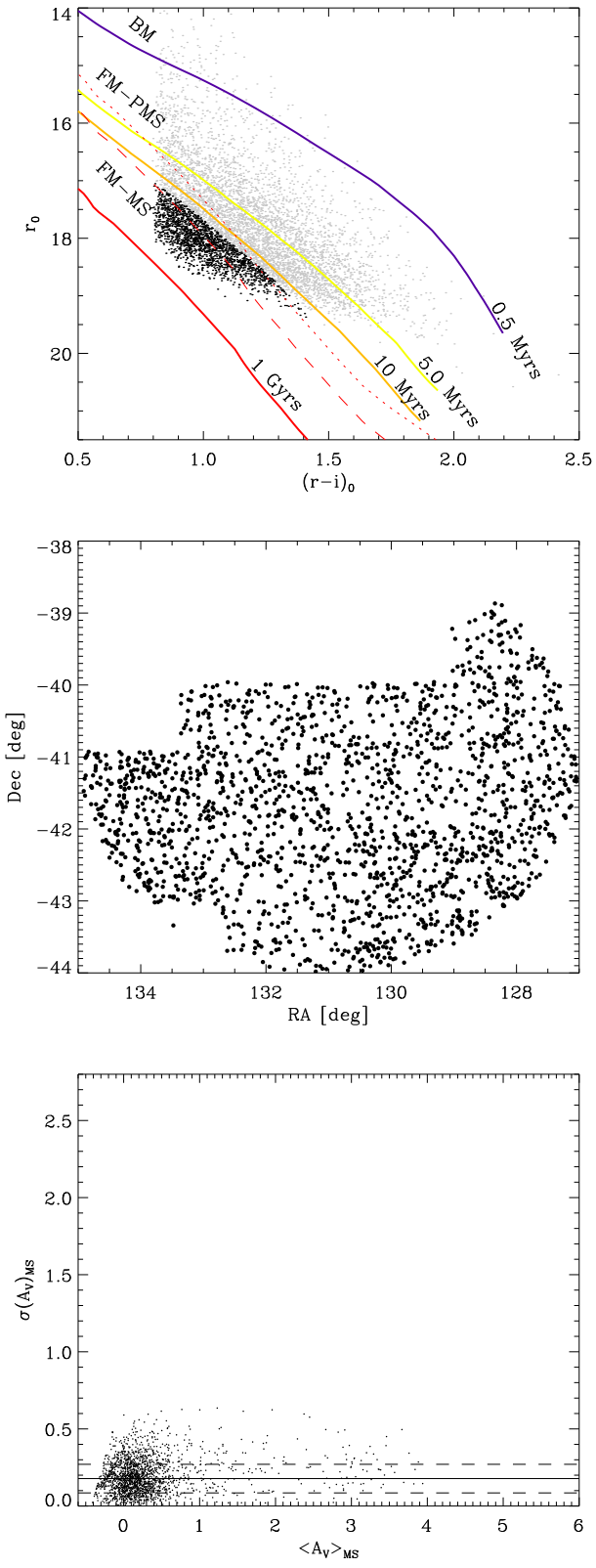

Fig. 17. r_0 vs. $(r-i)_0$ diagram of the faint M-type population (*upper panel*). Black dots show those selected as MS foreground field stars (see text). The solid lines show the 0.5, 5.0, 10.0 Myr and the 1 Gyr isochrones at the cluster distance. Dotted and dashed lines represent the 1 Gyr isocrone at 300 and 400 pc, respectively. Spatial distribution (*middle panel*) and $\sigma(A_V)_{MS}$ (*bottom panel*) of the selected MS foreground field stars. The median and the median ± pseudo-σ of this distribution are indicated as the solid and dashed lines.

[7] M-type MS stars at distance smaller than 300–400 pc, in contrast, are expected to be brighter and therefore overlapping with the PMS region at the cluster distance.

described above, this FM-PMS population is expected to include the M-type members of the clusters, but also a fraction of contaminating field stars at distance smaller than about 300–400 pc. The spatial distribution of this sample, shown in Fig. 18, shows several clumps of stars, with a pattern very similar to the one found for the YSOs selected with classical methods (see Fig. 9), and this suggests that the genuine M-type YSOs are mainly distributed within the spatial strip drawn in the upper panel of Fig. 18 with red symbols. In contrast, the spatial distribution of the objects outside the strip is quite homogeneous. As a first approximation, we therefore assume that the FM-PMS within the strip is dominated by the young cluster members, while the FM-PMS outside the strip is dominated by the field star population. Figure 18 also shows the histograms of the A_V values for these two populations and for the MS foreground field stars. It is evident that the population dominated by the young cluster members shows two peaks, centered at about $A_V \sim 0.3$ and $A_V \sim 1.5$, while the other two populations, dominated by the field stars, are both very similar and show a single peak at about $A_V = 0.3$, with a rapid decrease for $A_V \gtrsim 1$. The A_V distribution of the young cluster members shows a minimum at $A_V = 0.9$, corresponding to a sharp drop in the two field distributions. This is the A_V limit that clearly separates the young population from the field population. We cannot exclude that a small fraction of YSOs might be affected by reddening lower than $A_V = 0.9$ and vice versa, that a small fraction of MS field stars might be affected by $A_V > 0.9$, like the cluster stars. Nevertheless, the inclusion of this very small fraction of contaminants and the potential loss of a few reddened YSOs do not affect our results.

Based on this finding, we split the FM-PMS population into two subsamples, one including objects with $A_V > 0.9$, and the other including the objects with $A_V \leq 0.9$, to which we refer as red-FM-PMS and near-FM-MS populations.

Figure 19 shows the spatial distributions of the red-FM-PMS and the near-FM-MS populations. The spatial pattern of the red-FM-PMS population is very similar to that of members selected with other membership criteria (see Fig. 12), and therefore we deduce that the large majority of these objects are genuine members of the three young clusters in RCW 33, RCW 32, and RCW 27. As found with other methods, some candidate members are still sparsely distributed in the regions outside. Even though they could be less-likely members, we did not attempt to discard them since the shape of the clumps with a high density of cluster members is very irregular, and we cannot discard the hypothesis that many of them are true YSOs. Therefore, we kept all objects of the red-FM-PMS sample as M-type candidate cluster members. We note that the sample of 907 cluster members, previously selected with classical methods, includes only 84 M-type stars. Of these, 72 (8) belong to the red-FM-PMS (near-FM-MS) populations and are therefore confirmed cluster members. Based on the A_V distribution, we know that a small fraction of cluster members is expected to also belong to the near-FM-MS population, mainly populated by non-members. Only three objects belong to the population of foreground stars, and one belongs to the BM population.

A very different spatial distribution is found for the near-FM-MS population instead. It is quite uniform, even though there is a slightly higher stellar density around RA = 131.°8 and Dec = −42.°4, which corresponds to the nominal center of the Trumpler 10 association (Kharchenko et al. 2013). The result is better visible when we restrict the analysis to objects within a 0.5 mag strip around a 20 Myr isochrone at the distance of Trumpler 10 (422 pc) found with the PM analysis. However, since the spatial distribution of Trumpler 10 is very sparse, we did not attempt to select its members. Therefore, we classified all the objects belonging to the near-FM-MS population as objects not associated with the three young clusters.

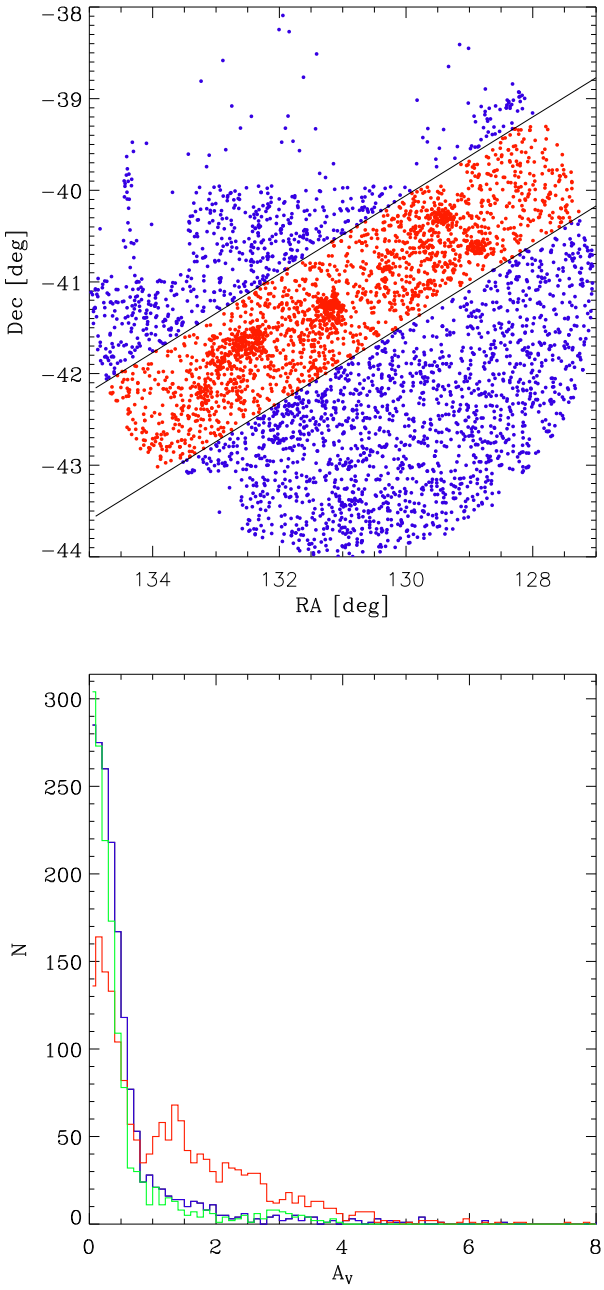

Fig. 18. *Upper panel*: spatial distribution of the FM-PMS population, divided into two samples, internal (red points) and external (blue point) to the strip arbitrarily defined by the two solid lines. *Bottom panel*: histograms of the A_V distribution obtained using the FM-PMS population within the strip (red histogram), FM-PMS population outside the strip (blue histogram), and the MS foreground field stars (green histogram).

In summary, we have selected 627 objects belonging to the M-type bright population and 6462 objects of the M-type faint population, for which we derived the individual interstellar reddening. The objects in the faint population include 1869 foreground field MS stars with distances larger than 300–400 pc, 3393 near-FM-MS stars within the PMS photometric region that are affected by low reddening that are not correlated to the young clusters, and finally 1200 FM-PMS stars that we consider as M-type candidate members of the young clusters.

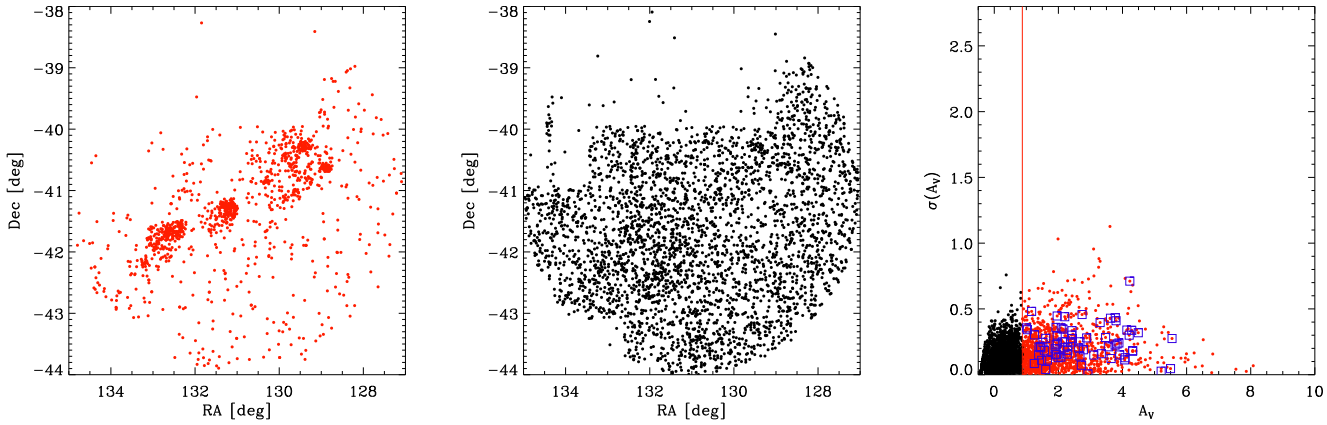

Fig. 19. Spatial distributions (*left and middle panels*) and $\sigma(A_V)$ vs. A_V (*right panel*) associated with each star belonging to the red-FM-PMS (red dots) and near-FM-MS (black dots) populations. Blue squares represent the objects with disks selected from IR and/or Hα excesses.

Figure 19 also shows the $\sigma(A_V)$ as a function of A_V for the red-FM-PMS and the near-FM-MS samples. In this figure, we highlight the YSOs with IR and/or Hα excesses, which are also selelcted as M-type stars. We find that very few of them show a $\sigma(A_V)$ significantly larger than the other objects, while the remaining show a $\sigma(A_V)$ distribution very similar to that of the other members. This result suggests that for the M-type members, the effects due to the presence of circumstellar disk on the A_V values derived with this method can be considered negligible.

8. Discussion

8.1. Spatial distribution analysis

The large number of likely M-type PMS stars selected in this work is consistent with results recently discussed in Damiani (2018) and is related to the higher intrinsic brightness of PMS M-type stars with respect to MS M-type stars. This implies that at a given mass, a 1 Myr old M star can be detected at a distance much larger than an MS M star (Damiani 2018). This is a very important property of M-type stars, which has been little exploited up to now in the literature, and which can instead be used as a very efficient tool for detecting the low-mass population of YSOs in star-forming regions, which is dominated by M-type stars. In addition, by deriving the individual reddening values using different optical-IR color combinations and the model predictions for different ages, we are able to separate MS and giant M-type stars, which are mainly expected to be found at small and large distances from us, respectively, and to recognize M-type YSOs.

This result is confirmed from the spatial distributions shown in Fig. 20 for the M-type young cluster members and for the members selected with classical methods. The colored maps are two-dimensional histograms to which we applied a smoothing with a Gaussian kernel.

The comparison of the two spatial distributions shows a clear spatial correlation between the YSOs selected with classical methods and the M-type candidate members selected in Sect. 7.2.2, confirming the peculiar patterns of the three regions, with a more concentrated distribution of YSOs in Cr 197 (RCW 32). The spatial distribution of objects in the cluster Vela T2 (RCW 33) is slightly more sparse with an ellipsoidal shape, and that in Vela T1 (RCW 27) is very sparse with evidence of several clumps. We verified that the spatial distribution of the faint FM-MS population and that of the objects selected as near-FM-MS and BM (background) giants are not indicative of any significant stellar density clumps, but rather are consistent with a uniform and homogeneous distribution.

8.2. SF history of M-type stars

For the M-type YSOs, we computed stellar ages assuming the distance d = 750 pc and using the individual reddening values derived in Sect. 7. A minimum and a maximum value to stellar ages was estimated by considering the photometric errors on r and i and the error on A_V. The A_V and stellar ages of M-type members together with their coordinates and optical/NIR photometry are given in Table 3. Figure 21 shows the intrinsic r_0 versus $(r-i)_0$ diagrams and the age distributions of the members within the three regions with the highest density, defined in Table 4. Objects were separated into three age ranges: $t < 2$ Myr, $2 < t/\mathrm{Myr} < 5$, and $t > 5$ Myr. The age distributions of the three clusters show a similar spread with ages from 0.5 to about 13 Myr, but the population of RCW 27 seems to contain a double generation of YSOs, one with a median age of about 2–3 Myr, and another with a median age of about 5–6 Myr. Figure 22 shows the spatial distributions of the YSOs selected with the classical methods and the M-type YSOs distinguished in the same three age ranges as defined above, compared with the dust distribution shown by the IR WISE images at 12 μm in the three regions with the highest density. The position of the ionizing stars and known clouds in the region are given in Table 5. For each of the three clusters, Vela T2, Cr 197, and Vela T1, and following the approach of Fasano & Franceschini (1987) , we applied the Kolmogorov-Smirnov (K-S) test on two samples and two dimensions to the spatial distributions of each pair of subgroups of YSOs with different age. We determined the probability of them being extracted from the same parent distribution, as reported in Table 6, where the p-values are given for each region. We discuss these probabilities in the following sections.

8.2.1. Vela T2 and RCW 33

The WISE image shows two bright clouds, corresponding to the $C^{18}O$ clouds 14 and 15 of Yamaguchi et al. (1999b) and several bright rimmed clouds (BRC). The two ionizing stars HD 75759 and HD 75724 lie in the southern region. The first is a binary with spectral type O9V+B0V, and the second is a B2III star. The first generation of stars ($t > 5$Myr) are found along the direction defined by clouds 14 and 15, with a higher concentration of stars between the two ionizing stars and cloud 14. The second

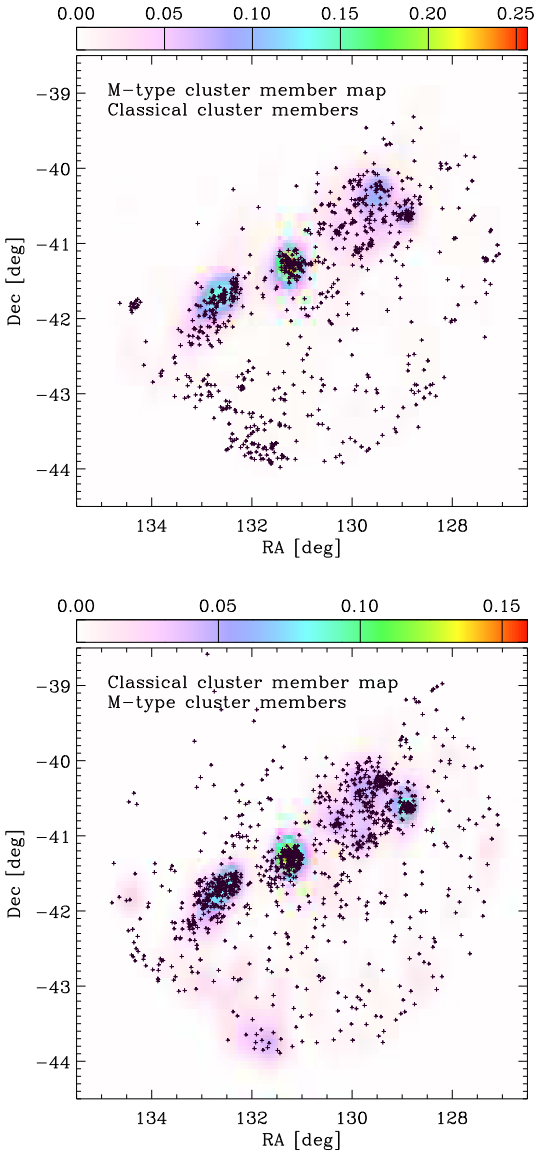

Fig. 20. *Upper panel*: spatial distribution of cluster members selected as M-type PMS stars in Sect. 7.2.2, plotted as a two-dimensional histogram smoothed with a Gaussian kernel. The density scale is the number of stars per bin and per arcmin^2. Overplotted black crosses are candidate members selected with classical methods. *Lower panel*: spatial distribution of cluster members selected with classical methods, plotted as a smoothed two-dimensional histogram. Overplotted black crosses are cluster members selected as M-type PMS stars.

generation of stars ($2 < t$/Myr < 5) are mostly found in the same region following the same pattern, and the youngest stars ($t < 2$ Myr) mostly formed two clumps around clouds 14 and 15, with a few more stars in the middle region, which seems to follow the pattern defined by the dust density enhancements. The difference between the spatial distributions of the subgroups is not significant or only marginally significant, with p-values of between 0.04 and 0.5.

8.2.2. RCW 32 and Cr 197

In the region of RCW 32, cluster members are found between the SFO 58 and SFO 57 BRCs (Sugitani & Ogura 1994), associated with the B0 V-B4 II ionizing star HD 74804 (Urquhart et al. 2009). Both SFO57 and SFO58 are included in the sample of candidates for triggered SF (Urquhart et al. 2009), associated with the formation of a photon-dominated region. Our results show that the first generation of stars formed a clump around HD 74804 and another group on the western side, along the direction of SFO 58 and attached to it, while the second generation formed in the middle region between the two BRCs. The few stars formed in the last 2 Myr are concentrated around HD 74804 and in the proximity of the two BRCs. However, the difference between the spatial distributions of the subgroups is not significant, with p-values of between 0.06 and 0.2.

8.2.3. Vela T1 and RCW 27

In the region of RCW 27, the first generation of stars are found in a clump around (RA, Dec) = (129.25, −40.25) deg, and other stars, some of which are concentrated along the bow-shape pattern formed by the dust, limited by the SFO 55 BRCs and the reflection nebula NGC 2626, and a second small group of stars, with an elongated distribution, around (RA, Dec) = (129.87, −41.17). The second generation of stars formed two other small clumps of stars in the proximity of the O8.5IV star HD 73882, a prominent clump around the reflection nebula NGC 2626 and a small clump around SFO 55. More recent SF occurred around NGC 2626, around (RA, Dec) = (129.87, −41.17), and again along the bow-shape pattern formed by the dust around (RA, Dec) = (129.7, −40.65), going up along the filament formed by the dust. In this region, the difference between the spatial distributions of the first and the second generation of stars is marginally significant (p-value = 0.04), but the difference between the spatial distributions of the youngest stars and the other groups is significant, with a p-value = 0.00006 in both cases.

8.2.4. Concluding remarks

The spatial distribution of the M-type members suggests that several clumps formed in correlation with stellar ages, revealing that SF in young clusters occurs in small subclusters, as predicted by models (Clarke et al. 2000).

For the YSOs selected with the classical methods we are not able to derive accurate individual reddenings and therefore ages. However, the spatial distribution of these objects is consistent with a population formed as the M-type selected members. The spatial distribution of most YSOs in RCW 33 is consistent with that found for the first generation of M-type stars, while that of YSOs in RCW 32 and RCW 27 is better consistent with the one found for the second generation of M-type stars.

Our results suggest a significant age spread with evidence of a continuous SF process that started about 12–13 Myr ago and lasted until less than 1 Myr ago. The age distribution in the three regions is consistent with a decreasing SF rate only in Vela T2 (RCW 33), while the age distribution of YSOs in Cr 197 (RCW 32) might suggest the presence of a triggering process likely due to the ionizing star HD 74804, which is consistent with the scenario suggested by Urquhart et al. (2009), in which the H II region radiation causes the compression and the fragmentation of the material in the molecular cloud.

Strong evidence of triggered SF has also been found in Vela T1 (RCW 27), where several clumps formed with time. The two peaks in the age distribution suggest an SF acceleration that is likely caused by the physical interaction between the radiation of massive stars and the surrounding molecular cloud.

To estimate the total number of stars and the total mass of the three populations, we assumed a universal initial mass

Table 3. Optical/NIR photometry, A_V, and ages of M-type members.

CNAME	RA (J2000)	Dec (J2000)	r	i	J	H	K	A_V (mag)	Log(t) (yr)	Log(t)$_{min}$ (yr)	Log(t)$_{max}$ (yr)
08475118 – 3928303	131.96325	−39.47508	14.90	13.87	11.73	10.99	10.72	1.13 ± 0.08	5.00	5.00	5.04
08572585 – 4026000	134.35771	−40.43334	15.85	14.77	12.59	11.78	11.50	1.28 ± 0.04	5.62	5.52	5.67
08575042 – 4032562	134.46010	−40.54893	15.06	14.00	11.86	11.06	10.81	1.16 ± 0.02	5.00	5.00	5.00
08472297 – 3816088	131.84571	−38.26911	15.27	14.07	11.71	10.79	10.49	1.62 ± 0.05	5.00	5.00	5.00
08363711 – 3824341	129.15461	−38.40948	15.58	14.51	12.41	11.58	11.36	0.91 ± 0.01	5.53	5.50	5.56
08372719 – 4153363	129.36330	−41.89341	14.55	13.41	11.04	10.27	9.91	1.69 ± 0.12	5.02	5.00	5.15
08372719 – 4153363	129.36330	−41.89341	14.55	13.41	11.04	10.27	9.91	1.69 ± 0.12	5.02	5.00	5.15
08372719 – 4153363	129.36330	−41.89341	14.55	13.41	11.04	10.27	9.91	1.69 ± 0.12	5.02	5.00	5.15
08360090 – 3941072	129.00376	−39.68533	15.40	14.05	11.28	10.35	9.95	2.74 ± 0.06	5.04	5.00	5.10
08384800 – 4202113	129.69999	−42.03646	15.69	14.56	12.20	11.59	11.32	1.35 ± 0.36	5.19	5.06	6.27
08310898 – 3926229	127.78741	−39.43969	16.06	14.82	12.35	11.49	11.17	1.93 ± 0.02	5.03	5.00	5.11

Notes. The full table is available at the CDS.

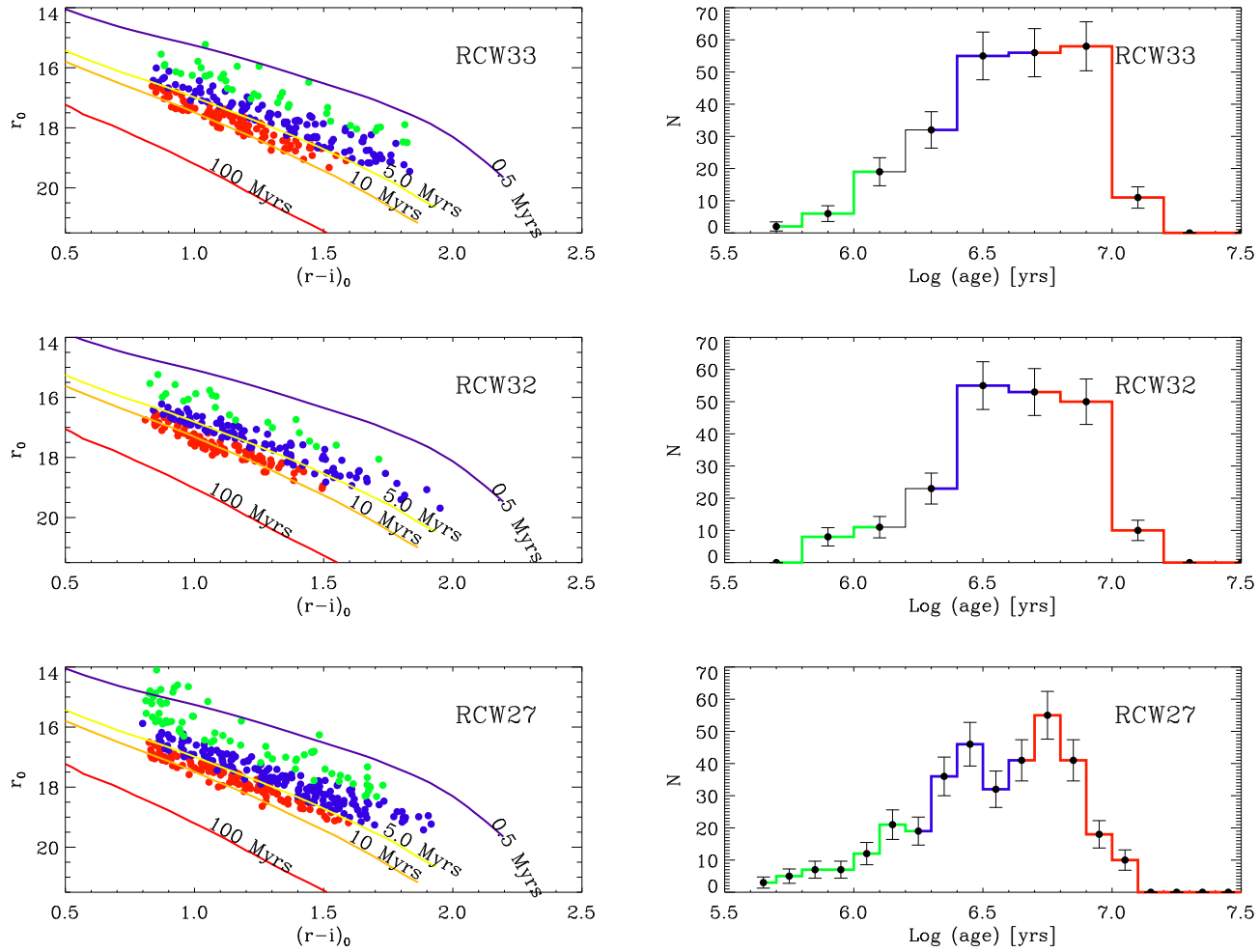

Fig. 21. Intrinsic CMDs and age distributions of the M-type candidate members falling in the three regions defined in Table 4 and grouped into three age ranges, i.e., $t < 2$ Myr, $2 < t/[\mathrm{Myr}] < 5$, and $t > 5$ Myr, indicated with green, blue, and red symbols, respectively. Several representative isochrones are overplotted in the CMD.

function (IMF) and considered the completeness limits of the magnitudes for M-type stars. These are $r = 19.97$, $i = 19.09$, $J = 15.87$, $H = 15.09$, and $K = 14.4250$. These values were estimated at the peak of the magnitude distribution. As described in Damiani (2018), the minimum mass detected at a given distance strongly depends on the age and the absorption A_V (see Fig. 5 of Damiani 2018). To estimate the lowest mass above which our sample is complete, we used two isochrones at two representative ages for the three regions, that is, 4 and 5 Myr, and the median A_V of the three regions, which are $A_V^{med} = [1.4, 2.5, 1.8]$ for RCW 33, RCW 32, and RCW 27, respectively. Under these conditions, we estimate that the mass ranges in which M-type stars younger than 4 and 5 Myr with $A_V < A_V^{med}$ are all detected are [0.22−0.94] $M_\odot$, [0.34−0.94] $M_\odot$, and [0.27−0.94] $M_\odot$ for 4 Myr

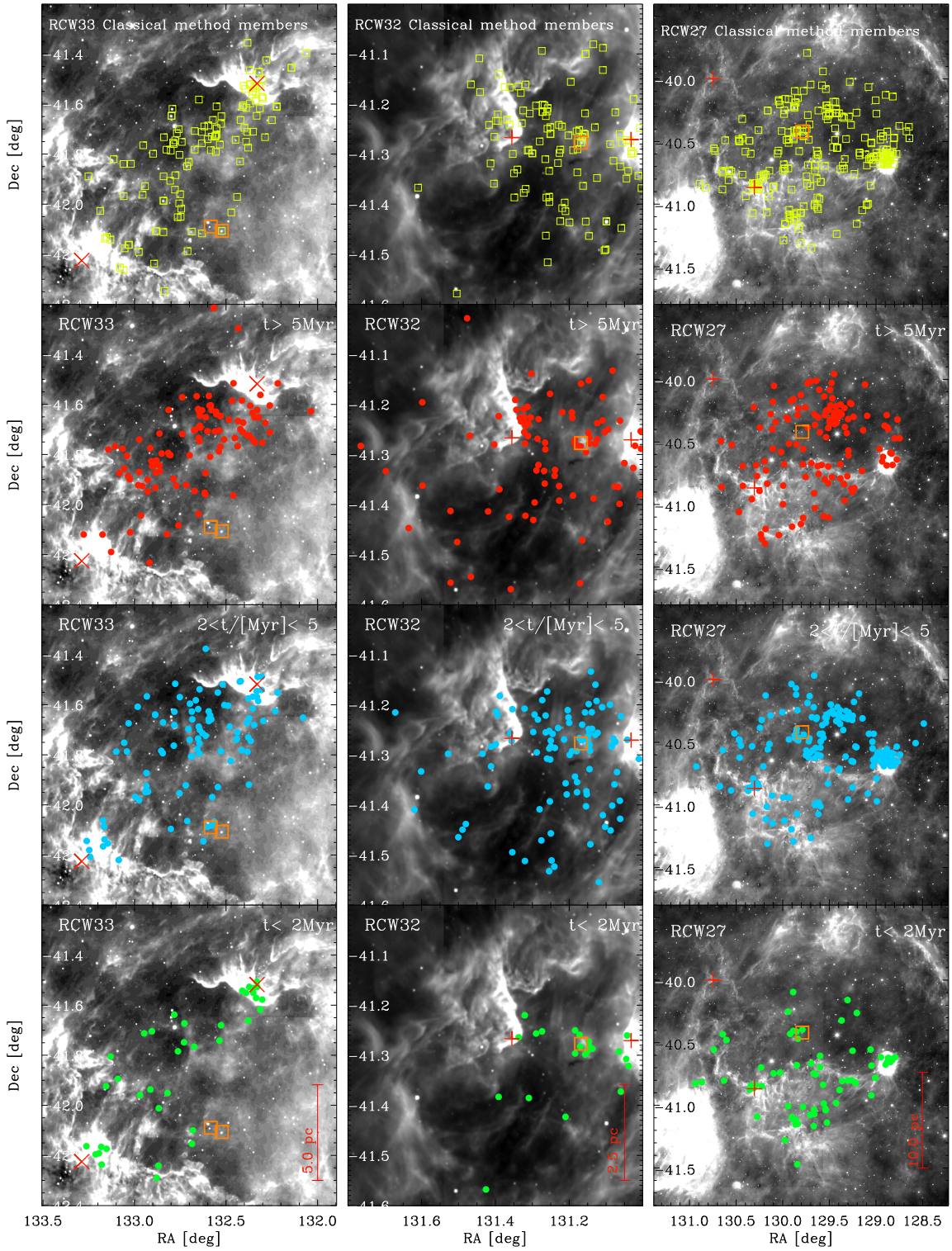

Fig. 22. Different scale WISE images at 12 μm in RCW 33, 32, and 27 in the *left, middle and right panels*, respectively. YSOs selected with classical methods (*upper panels*) and M-type YSOs in different age ranges (*lower panels*) are overplotted with yellow squares and red, blue, and green points, respectively. Orange empty squares indicate the position of the ionizing stars, and red crosses and pluses correspond to $C^{18}O$ clouds 14 and 15 and to SFO sources, respectively.

and [0.24−0.94] $M_\odot$, [0.36−0.94] $M_\odot$, and [0.28−0.94] $M_\odot$ for 5 Myr for RCW 33, RCW 32, and RCW 27, respectively. The upper bound of the mass ranges were derived from the 4 and 5 Myr isochrones for $i-K > 2.2$, which is the color limit used for the selection of M-type stars (see Fig. 13).

In these ranges, the oldest and more reddened objects cannot be detected. For each of the three clusters, we counted the number of stars within these mass ranges with A_V lower than the median value of each region and ages younger than 4 (5 Myr), which are 30, 18, and 62 (42, 24, and 64) in RCW 33, RCW 32,

Table 4. Galactic coordinates of the boxes around the three H II regions with the highest star density.

H II	Min. l	Max. l	Min. b	Max. b
RCW33	262.0	263.2	1.2	1.8
RCW32	261.2	261.9	0.6	1.3
RCW27	259.5	261.1	−0.2	1.2

Table 5. Coordinates of the ionizing stars and of known clouds in the region.

H II	ID	RA (deg)	Dec (deg)
RCW33	HD 75759	132.58	−42.09
RCW33	HD 75724	132.52	−42.11
RCW32	HD 74804	131.17	−41.28
RCW27	HD 73882	129.79	−40.42
RCW33	Cloud 14	132.33	−41.52
RCW33	Cloud 15	133.29	−42.23
RCW32	SFO58	131.36	−41.27
RCW32	SFO57	131.03	−41.27
RCW27	SFO56	130.75	−40.00
RCW27	SFO55	130.30	−40.87
RCW27	NGC 2626	128.88	−40.67

Table 6. *p*-values resulting from applying a two-sample K-S test to the spatial distributions of each pair of subgroups with different age.

H II	Age range 1 (Myr)	Age range 2 (Myr)	*p*-values
RCW 33	[0–2]	[2–5]	0.05
RCW 33	[2–5]	[5–13]	0.5
RCW 33	[0–2]	[5–13]	0.04
RCW 32	[0–2]	[2–5]	0.2
RCW 32	[2–5]	[5–13]	0.15
RCW 32	[0–2]	[5–13]	0.06
RCW 27	[0–2]	[2–5]	0.00006
RCW 27	[2–5]	[5–13]	0.04
RCW 27	[0–2]	[5–13]	0.00006

and RCW 27, respectively. To account for the objects in the same mass ranges, but with ages older than 4 and 5 Myr, we used the fraction of M-type stars in these mass ranges and within the same limits on A_V, but with ages older than 4 (5 Myr), which are 0.70, 0.69, and 0.53 (0.58, 0.55, and 0.47). Finally, we extrapolated the total number of stars of the three populations across the entire mass spectrum by considering the fraction of stars predicted by the Weidner et al. (2010) IMF in the same mass ranges, which are 0.34, 0.21, and 0.28 (0.32, 0.20, and 0.27). We thus estimate that the total number of YSOs for the three populations is in the range [124–224], [122–216], and [403–493] stars in RCW 33, RCW 32, and RCW 27, respectively. When we consider the total mass of M-type stars within the previous mass ranges and consider the mass fraction predicted in the same ranges with the Weidner et al. (2010) IMF, we estimate that the total mass of the three populations is [50−86] $M_\odot$, [45−81] $M_\odot$, and [141−174] $M_\odot$. The large uncertainties on these estimates are mainly due to the limited depth of the 2MASS photometry, which will hopefully be overcome by future deep IR surveys covering this region. We note that using the limit of 4 Myr, the mass ranges are slightly larger than using 5 Myr, and this allows us a slightly less uncertain extrapolation of the IMF. At the same time, however, we include a smaller fraction of objects in our computation, and a larger correction for older stars is therefore necessary. Thus, our choice to consider the two isochrones of 4 and 5 Myr enables us to obtain an estimate as reliable as possible, which should be considered with caution, however, and it is likely a lower limit since we did not apply a correction for YSOs with $A_V > A_V^{med}$.

9. Summary and conclusions

We used optical and NIR photometric surveys to study the young stellar population in the three H II regions RCW 33, 32, and 27, where Pettersson & Reipurth (1994) found signatures of recent SF from Hα observations. Using the deeper VPHAS+ survey, which covers the region studied by Pettersson & Reipurth (1994), we found 329 YSOs with Hα emission showing a spatial pattern that confirms the presence of young clusters associated with the three H II regions. This result prompted the search of the associated population of YSOs surrounded by a circumstellar disk through NIR surveys such as *Spitzer*/GLIMPSE and 2MASS. Using the known properties of YSOs with disks, we selected 559 Class II and 20 Class I YSOs. We exploited the recent *Gaia* DR1 to study the kinematic population of the three regions, and we found 10, 19, and 25 stars that share similar PMs and parallaxes in Cr 197, Vela T2, and Vela T1, respectively, confirming the presence of the three clusters, with a placement in the CMD consistent with PMS stars at the distance of about 750 pc. The distance of the three regions derived from the *Gaia* data is consistent with that derived from the CMD of the low-mass population. Additional YSOs were found using also archive ROSAT and *Chandra* X-ray observations. We finally selected a total of 907 candidate YSOs in the whole region, with different spatial distribution patterns in the three H II regions.

We added to this sample another sample of 1 200 candidate M-type members. These objects were selected by exploiting two important features of M-type stars: the significantly higher luminosity in the PMS phase with respect to MS stars of the same spectral type, and the sensitivity of their $i-J$, $i-H$, and $i-K$ colors to stellar gravity. This allowed us to derive the individual reddening independently in three different CCDs, and to select the best A_V value for each M-type star. For the whole M-type population, including the field star population, we therefore derived the unreddened CMD where the only unknown is the distance.

The comparison of the unreddened CMD with PMS isochrones at the distance of the clusters allowed us to discard the foreground population of M-type MS stars and the background population of M-type giants. In addition, based on the spatial analysis, we found that the populations of YSOs in RCW 33, 32, and 27 are dominated by objects with $A_V > 1$, and this allowed us to also discard the low-reddening ($A_V > 1$) population of M-type MS stars that contaminated the photometric PMS locus in the CMD of the clusters.

The spatial distribution of the M-type YSOs is strongly correlated with that of the YSOs selected with classical methods. Since we have a subsample of 72 M-type stars selected with both methods, we find a total population of 2 035 YSOs, mainly distributed inside the three H II regions, presenting for the first time a stellar census of YSOs in NW-VMR down to M-type stars. For the M-type YSO subsample, we also derived stellar masses down to 0.1 $M_\odot$ and stellar ages in the range 0.5–13 Myr.

We performed a detailed spatial analysis of the M-type members in the three H II regions and compared them with WISE images at 12 μm, which highlights the regions with a high

concentration of dust. By splitting the M-type YSOs into three different age ranges, we found indications on the SF rate. In particular, we found that the formation of YSOs in clumps or in elongated features is connected to the ages and to BRCs, which are visible in the WISE image.

The most likely scenario is that while the SF rate in RCW 33 is decreasing with time, the SF process in RCW 32 and 27 has likely been triggered by the interaction between the H II radiation associated with the ionizing stars and the molecular clouds from which the low-mass star population formed. This scenario is consistent with that suggested by Urquhart et al. (2009) based on CO and mid-IR observations of a sample of H II regions, including RCW 32 and RCW 27.

The criteria used in this work to select M-type stars can be exploited in future works in several contexts of stellar astrophysics. In the context of SF, the intrinsic higher luminosity of M-type stars in PMS phase with respect to MS stars is a new observational diagnostics that allows detection of the M-type young populations of relatively distant regions ($\sim$1−2 kpc) using recent photometric surveys. The M-type population in these regions has up to now been mainly revealed by deep and highly sensitive X-ray or spectroscopic observations, which are significantly more expensive in terms of telescope time. In addition, the limited FOV makes it very difficult, if not impossible, to study large fields of several square degrees, which can be easily done with the current photometric surveys.

The *Gaia* DR2 data will likely allow more refined selections because the kinematic parameters will enable confirming M-type candidate members. Moreover, other available and future very deep photometric surveys, such as PanSTARRS, UKIDSS, WISE, VVV, and LSST, will allow us to detect even more distant M-type stars in even more distant star-forming regions.

Finally, the opportunity for deriving accurate individual reddening values of M-type stars is a new tool that can be exploited to discard M-type contaminants, both MS or giants, and therefore to select M-type members based on the known parameters of the clusters we study. Moreover, this new diagnostic can be exploited to distinguish M-type MS stars from giants in fields where YSOs are not expected to be found.

Acknowledgements. We wish to thank the anonymous referee for his/her interesting comments and suggestions. This work is based on observations made with ESO Telescopes at the La Silla or Paranal Observatories under programme ID(s) 177.D-3023(B), 177.D-3023(C), 177.D-3023(D), 177.D-3023(E). This work has made use of data from the European Space Agency (ESA) mission *Gaia* (http://www.cosmos.esa.int/gaia), processed by the *Gaia* Data Processing and Analysis Consortium (DPAC, http://www.cosmos.esa.int/web/gaia/dpac/consortium). Funding for the DPAC has been provided by national institutions, in particular the institutions participating in the *Gaia* Multilateral Agreement. This publication makes use of data products from the Wide-field Infrared Survey Explorer, which is a joint project of the University of California, Los Angeles, and the Jet Propulsion Laboratory/California Institute of Technology, funded by the National Aeronautics and Space Administration.

References

Benjamin, R. A., Churchwell, E., Babler, B. L., et al. 2003, PASP, 115, 953
Bonatto, C., & Bica, E. 2010, A&A, 516, A81
Cardelli, J. A., Clayton, G. C., & Mathis, J. S. 1989, ApJ, 345, 245
Churchwell, E., Babler, B. L., Meade, M. R., et al. 2009, PASP, 121, 213
Cieza, L. A., Kessler-Silacci, J. E., Jaffe, D. T., Harvey, P. M., & Evans, II, N. J. 2005, ApJ, 635, 422
Clarke, C. J., Bonnell, I. A., & Hillenbrand, L. A. 2000, Protostars and Planets IV, 151
Crampton, D., & Fisher, W. A. 1974, Publications of the Dominion Astrophysical Observatory Victoria, 14, 283
Cutri, R. M., Skrutskie, M. F., van Dyk, S., et al. 2003, The IRSA 2MASS All-Sky Point Source Catalog, NASA/IPAC Infrared Science Archive, http://irsa.ipac.caltech.edu/applications/Gator/
Damiani, F. 2018, A&A, 615, A148
Damiani, F., Pillitteri, I., & Prisinzano, L. 2017, A&A, 602, A115
de Zeeuw, P. T., Hoogerwerf, R., de Bruijne, J. H. J., Brown, A. G. A., & Blaauw, A. 1999, AJ, 117, 354
Dias, W. S., Alessi, B. S., Moitinho, A., & Lépine, J. R. D. 2002, A&A, 389, 871
Drew, J. E., Gonzalez-Solares, E., Greimel, R., et al. 2014, MNRAS, 440, 2036
Fasano, G., & Franceschini, A. 1987, MNRAS, 225, 155
Gaia Collaboration (Brown, A. G. A., et al.) 2016a, A&A, 595, A2
Gaia Collaboration (Prusti, T., et al.) 2016b, A&A, 595, A1
Gaustad, J. E., McCullough, P. R., Rosing, W., & Van Buren, D. 2001, PASP, 113, 1326
Georgelin, Y. M., Georgelin, Y. P., & Roux, S. 1973, A&A, 25, 337
Gutermuth, R. A., Megeath, S. T., Myers, P. C., et al. 2009, ApJS, 184, 18
Henden, A. A., Templeton, M., Terrell, D., et al. 2016, VizieR Online Data Catalog: II/336
Indebetouw, R., Mathis, J. S., Babler, B. L., et al. 2005, ApJ, 619, 931
Kenyon, S. J., & Hartmann, L. 1995, ApJS, 101, 117
Kharchenko, N. V., Piskunov, A. E., Röser, S., Schilbach, E., & Scholz, R.-D. 2005, A&A, 440, 403
Kharchenko, N. V., Piskunov, A. E., Schilbach, E., Röser, S., & Scholz, R.-D. 2013, A&A, 558, A53
Liseau, R., Lorenzetti, D., Nisini, B., Spinoglio, L., & Moneti, A. 1992, A&A, 265, 577
Lorenzetti, D., Spinoglio, L., & Liseau, R. 1993, A&A, 275, 489
Marigo, P., Girardi, L., Bressan, A., et al. 2017, ApJ, 835, 77
Massi, F., Giannini, T., Lorenzetti, D., et al. 1999, A&AS, 136, 471
Massi, F., Lorenzetti, D., & Giannini, T. 2003, A&A, 399, 147
Massi, F., Testi, L., & Vanzi, L. 2006, A&A, 448, 1007
Meyer, M. R., Calvet, N., & Hillenbrand, L. A. 1997, AJ, 114, 288
Murphy, D. C., & May, J. 1991, A&A, 247, 202
O'Donnell, J. E. 1994, ApJ, 422, 158
Oke, J. B., & Gunn, J. E. 1983, ApJ, 266, 713
Olmi, L., Ade, P. A. R., Anglés-Alcázar, D., et al. 2009, ApJ, 707, 1836
Pettersson, B. 2008, Young Stars and Dust Clouds in Puppis and Vela, ed. B. Reipurth, 43
Pettersson, B., & Reipurth, B. 1994, A&AS, 104, 233
Randich, S., Tognelli, E., Jackson, R., et al. 2018, A&A, 612, A99
Stetson, P. B. 1987, PASP, 99, 191
Sugitani, K., & Ogura, K. 1994, ApJS, 92, 163
Testi, L., Vanzi, L., & Massi, F. 2001, The Messenger, 103, 28
Tognelli, E., Prada Moroni, P. G., & Degl'Innocenti, S. 2011, A&A, 533, A109
Urquhart, J. S., Morgan, L. K., & Thompson, M. A. 2009, A&A, 497, 789
Wang, S., Liu, J., Qiu, Y., et al. 2016, ApJS, 224, 40
Weidner, C., Kroupa, P., & Bonnell, I. A. D. 2010, MNRAS, 401, 275
Yamaguchi, N., Mizuno, N., Saito, H., et al. 1999a, PASJ, 51, 775
Yamaguchi, R., Saito, H., Mizuno, N., et al. 1999b, PASJ, 51, 791
Zasowski, G., Majewski, S. R., Indebetouw, R., et al. 2009, ApJ, 707, 510